Time-Stretched Multi-Hit 3D Velocity Map Imaging of Photoelectrons

E. Scott Goudreau,[1, 2, a)] Andrey E. Boguslavskiy,[1, 3, 2] Douglas J. Moffatt,[2] Varun Makhija,[1, 4] Michael Hemsworth,[1] Rune Lausten,[2] Claude Marceau,[2] Iain Wilkinson,[5, b)] and Albert Stolow[1, 3, 2, 6, c)]

[1)] *Department of Physics, University of Ottawa, Ottawa, Ontario, K1N 6N5, Canada*

[2)] *National Research Council Canada, Ottawa, Ontario, K1A 0R6, Canada*

[3)] *Department of Chemistry, University of Ottawa, Ottawa, Ontario, K1N 6N5, Canada*

[4)] *Department of Physics, University of Mary Washington, Fredericksburg, VA 22401, United States of America*

[5)] *Institute for Electronic Structure Dynamics, Helmholtz-Zentrum Berlin für Materialien und Energie, Hahn-Meitner-Platz-1, D-14109 Berlin, Germany*

[6)] *NRC-uOttawa Joint Centre for Extreme Photonics, Ottawa, Ontario, Canada*

The 2D photoelectron velocity map imaging (VMI) technique is commonly employed in gas-phase molecular spectroscopy and dynamics investigations due to its ability to efficiently extract photoelectron spectra and angular distributions in a single experiment. However, the standard technique is limited to specific light-source polarization geometries. This has led to significant interest in the development of 3D VMI techniques which are capable of measuring individual electron positions and arrival times, obtaining the full 3D distribution without the need for inversion, forward-convolution, or tomographic reconstruction approaches. Here we present and demonstrate a novel time-stretched, 13-lens 3D VMI photoelectron spectrometer which has sub-camera-pixel spatial resolution combined with 160 ps time-of-flight (TOF) resolution. We employ a kHz CMOS camera to image a standard 40 mm diameter MCP/phosphor anode detector (providing x and y positions), combined with a GHz digitizer pick-off from the MCP anode to obtain the electron TOF. We present a detailed analysis of time-space correlation under data acquisition conditions which generate multiple electrons per laser shot, and demonstrate a major advantage of this time-stretched 3D VMI approach: that the greater spread in electron TOFs permits an accurate time- and position-stamping of up to six electrons per laser shot at a 1 kHz repetition rate.

I. INTRODUCTION

Velocity Map Imaging (VMI)[1] has become a standard technique for making energy- and angle-resolved measurements of dissociation, non-reactive and reactive scattering, and ionization processes[2–8]. VMI was devised as an evolution of ion imaging[9], adding non-uniform fields to minimize the effect of the origin point of ions/electrons within the ionization volume, thus improving energy resolution. In a conventional VMI experiment, the ion or electron Newton sphere is projected onto a 2D position-sensitive detector and integrated images are acquired over a large number of laser shots. These images are then transformed using Abel inversion or a similar algorithm to reconstruct the full 3D distribution. It is well known that Abel inversion can magnify and localize image noise and requires an axis of cylindrical symmetry in the plane of the 2D projection (i.e. the plane of the detector). The latter restricts the laser polarization geometry which can be used, in turn disallowing important classes of experiments such as pump-probe studies with crossed or magic-angle polarization geometries.

A number of approaches have emerged to address this limitation, as described in detail in a recent review paper[10], and the variety of techniques being developed highlights the importance of true inversion-free 3D VMI. For ion measurements, slice-imaging is a popular alternative[11–13], as the arrival time spread of an ion Newton sphere can be hundreds of nanoseconds. Electron measurements are more challenging, since the arrival time spread is typically only a few nanoseconds and fast electronic gating of the detector is technically demanding.

The 3D ion/electron distributions can also be obtained directly, without the need for inversion, by measuring the spatial and temporal coordinates of each event individually. This can be done with the use of delay-line anode detectors[14], which allow accurate measurement of both position and arrival time for individual events. Delay-line anode detectors are limited in their ability to handle multiple events per laser shot[15], which in turn impedes the speed of data collection, particularly for electron imaging, owing to the aforementioned narrow arrival time spread. An alternative is to use a fast camera to image the spatial position of events. However, since conventional CCD/CMOS cameras lack the needed time resolution, the time-stamping of events must be obtained by other means. As we demonstrate below, our 3D VMI implementation accurately stamps, in both time and position, up to six electrons per laser shot within a 30 ns arrival time window.

A pertinent example of such a camera-based 3D VMI technique, developed by Li and co-workers, involves mea-

[a)] Electronic mail: egoud097@uottawa.ca

[b)] Electronic mail: iain.wilkinson@helmholtz-berlin.de

[c)] Electronic mail: astolow@uottawa.ca

suring spatial positions using an MCP/phosphor and fast CMOS camera while simultaneously time-stamping each event using either a PMT[16] or a capacitive pickoff from the detector to a fast digitizer[17–22]. The latter variation was shown to have sufficient time resolution for 3D electron VMI[17] and has been used successfully for electron-ion[19,21] and electron-electron[18,20] coincidence measurements. A similar approach was developed by Picard and co-workers[23].

Recently, 3D VMI implementations[24–27] using the Timepix[28] series of event-driven camera sensors have shown promise as a way to circumvent the need for separate position and time measurements by time-stamping each event as it occurs. This approach is currently limited by the ~250 ps time resolution and 256×256 pixel spatial resolution of the third generation Timepix sensor, although the very recent fourth generation of Timepix[29] has a time resolution below ~200 ps with a 448×512 pixel array. An improved time resolution has been achieved by combining the (comparatively) rough time stamps of the Timepix3 sensor with more precise timing using a detector-pickoff and digitizer setup[25,26]. Furthermore, using a coaxial 5-element electron lens and 6-element ion lens, 3D photoelectron VMI was combined with coincident (or covariant) ion detection, allowing for high resolution photoelectron images to be correlated with their associated cation distributions[27].

Here we have implemented the CMOS camera and detector-pickoff method of Li *et al* for 3D photoelectron measurements. Our goal was to address one of the main challenges of 3D electron VMI: the short arrival time spread of the electron sphere which must be increased in order to improve spectrometer TOF resolution and multi-hit capability. Although the original VMI design made use of only three electrodes, we note that multi-element (i.e. thick) charged particle VMI lenses, first demonstrated in 2003[12], have been successfully implemented in various applications[14,30–32] including a recent photoelectron-photoion coincidence 3D VMI implementation[27]. Here we present a 3D VMI spectrometer with a 13-plate electrode stack, capable of significantly stretching the arrival time distribution while maintaining good VMI focusing conditions. Importantly, being CMOS camera-based, standard 2D VMI capability is retained. As we demonstrate here for 3D VMI, we have achieved a global (i.e. averaged over the MCP area) time-of-flight resolution of 160 ps in combination with a sub-pixel spatial resolution over a 512×512 pixel array, with possibilities for improvement on both fronts. Our approach benefits from the ability to make use of any sufficiently fast CMOS camera, reducing cost and enabling the freedom to customize the choice of camera to suit given experimental requirements. In this work, we demonstrate the significant benefits of time-stretching, with a focus on multi-hit performance, using three photoionization test cases (Xe, CH_3I, and $NO(A\,^2\Sigma^+)$).

II. EXPERIMENTAL SETUP AND METHODS

In 3D electron VMI, the full 3D photoemission distribution can be determined directly, without the need for inversion, by simultaneously measuring the 2D position and arrival time (TOF) of each photoelectron at an imaging detector. Typically, for the camera-based approach used here, a high gain microchannel plate (MCP) detector is used in combination with a phosphor anode screen and high-speed camera to determine the 2D position, while a capacitive anode pick-off from the phosphor determines the electron TOF[22]. The 2D position yields (x, y), whereas the TOF is directly related to z, the coordinate along the flight axis. A key advantage of 3D VMI over other 3D recoil momentum vector imaging techniques, such as those based on delay line anode detectors, is the ability to readily characterize multiple electron events per laser shot, as we demonstrate here. In this multi-event case, it is necessary to correctly match each 2D position with its corresponding TOF. This is achieved via correlations in the output charge variation of the MCP, represented by its pulse height distribution (PHD). The broad PHD, typically ~100% FWHM (Full Width at Half Maximum) for a two-plate chevron MCP, ensures that the amplified output charge from single events will sample a wide range of values. If an integrated 2D position signal and an integrated TOF signal correspond to the same total charge, they likely belong to the same event and are assigned to each other, thus yielding the 3D coordinates (x, y, t) of that event. Resolving the 2D position of each event is straightforward since two electrons rarely arrive at the same position on the MCP detector. Therefore, a key challenge in this multi-event approach is to resolve, in time, the individual electrons (which typically arrive within a few ns of each other) while maintaining the 2D velocity mapping conditions. In the following, we present the design considerations, testing and calibration of a new 3D VMI spectrometer based on a 13-plate electrode stack which stretches the photoelectron TOF distribution while retaining good 2D VMI focusing conditions.

A depiction of our final design is given in Fig. 1. A skimmed molecular beam is crossed by a focused laser, producing photoelectrons. These are imaged by 13-element electron lens stack (green) onto an MCP detector, with the grey cloud between the dotted lines representing the travelling 3D photoelectron distribution. For illustrative purposes, we imagine three representative photoelectrons travelling towards the MCP detector, where the subsequent electron avalanche events are 2D imaged by a real-time kHz CMOS camera (hits 1, 2, 3 in the right inset). Simultaneously, these three electron events are coupled out by a pick-off capacitor on the phosphor anode and accurately timed by a fast digitizer (hits 1, 2, 3 in the left inset). The key idea of 3D VMI is that, provided that the three 2D positions and the three arrival times can be correctly matched, their 3D lab frame initial velocity vectors can be simultaneously determined

without the need for inversion algorithms.

Summary of SIMION Simulations

We used the SIMION 8.0 charged particle optics simulation package to investigate photoelectron energy resolution and TOF spread for several different 3D VMI designs. The interaction region is defined by the intersection of a pulsed molecular beam, which travels along the TOF (z-axis) direction, and, in our experiments, a weakly focused (typically f = 75 cm) femtosecond- or picosecond-pulse-duration laser beam with its propagation vector, $\vec{k}$, aligned along the y-axis. The volume of this interaction region was modeled as a cylinder of length 2 mm and diameter 0.1 mm. In our simulations, the interaction region was Monte Carlo sampled as a 2D Gaussian distribution with 0.1 mm $1/e^2$ widths along the x and z (radial) coordinates of this cylinder, and as a uniform distribution over the 2 mm length of its y-axis (i.e. a uniform gas density approximation).

We sampled thousands of electron trajectories from isotropic photoelectron angular distributions with discrete kinetic energy values ranging from 0 to 5 eV. For each electron trajectory, the 2D position (x, y) at the MCP and the TOF (related to z) were recorded. To assess the VMI energy resolution, a standard 2D VMI energy resolution criterion was used. Electrons with kinetic energy E focus to a ring of radius r and width Δr at the MCP detector. We binned the 2D positions of all electrons into an image and performed a standard Abel inversion. The resulting spectrum was fitted with a Gaussian function to determine the peak width and position. We then took the centroid of the Gaussian as the 3D radius R, with ΔR being the FWHM. The photoelectron energy resolution is then given by $\Delta E/E = 2\Delta R/R$.

As our TOF resolution for a single electron event is limited by electronics and the transit time across the anode, it is advantageous to stretch, as much as possible, the arrival time distribution. For this reason, the effective electron TOF resolution was characterized by the arrival time difference between the first and last electrons (using an isotropic photoelectron angular distribution) to hit the MCP. This turn-around time spread (TTS) is largely determined by the electric field strength in the interaction region (the extraction field). In order to stretch the electron distribution in time, the extraction field strength must be reduced. However, other constraints apply, namely: (i) the extraction field must be strong enough that electrons emitted perpendicular to the TOF axis can still be collected and imaged on the MCP detector; and (ii) the VMI focusing condition must be maintained.

The details and results of the SIMION simulations which led to the final 3D VMI design shown in Fig. 1 are presented elsewhere[33]. An important advantage of the 13-electrode design is in its significantly improved TTS. Although our full simulations involved thousands of

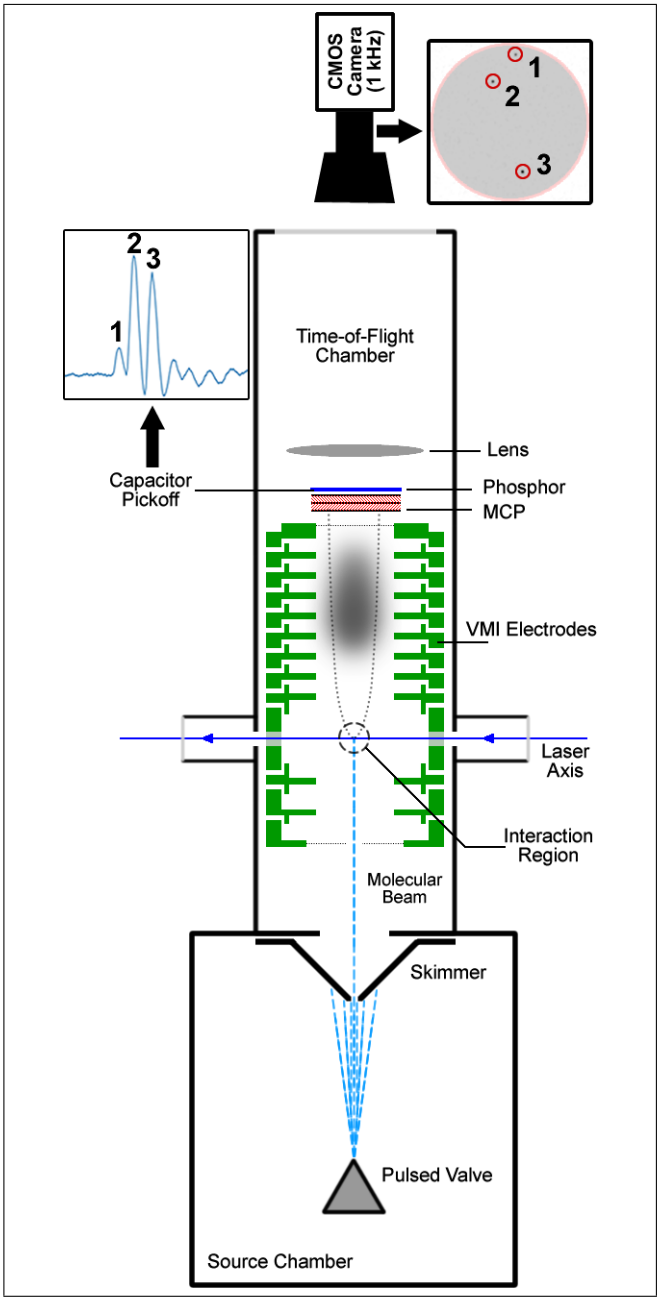

FIG. 1. Schematic layout of our 3D VMI spectrometer, illustrating the acquisition of three photoelectron events from a single laser shot in a 3D imaging experiment. A molecular beam originating from the pulsed valve located in the lower (source) chamber passes through a skimmer into the upper (time-of-flight) chamber where it is timed to intersect with laser pulses entering through a perpendicular port. Photoelectrons (grey cloud) are guided toward the MCP/phosphor detector by our novel 13-element VMI electrode stack (green) which extends the time-of-flight spread of the photoelectron distribution. Each electron event is detected simultaneously by both a high-speed camera (right inset) and a GHz digitizer connected to a capacitive anode pick-off from the phosphor (left inset). For each event, the 2D position from the camera and the corresponding time from the digitizer pulse are combined to give a 3D (x, y, t) coordinate for that event.

electron trajectories, a pedagogical discussion of selected SIMION results helps to illustrate this point. In Fig. 2, we present an expanded view of the 3D VMI spectrometer, showing the results of simulations (for 5 eV photoelectrons) discretely sampling the interaction region defined above. Exemplary SIMION electron trajectories (blue) are shown with illustrative electrons in transit (red dots), helping to visualize the improved electron TOF spread Δt. These trajectories were produced from a set of 9 electron origin points within this interaction volume (as shown in the lower left inset). Three horizontally displaced sets along the laser axis were located ±1 mm from, and exactly on, the cylindrically symmetric TOF (z) axis. Within each set, three origin points were placed ±50 μm from, as well as on, the laser axis. In this illustrative figure, each origin point spawned eight electron trajectories (blue) with initial velocities of equal magnitude sampling, in 45 degree steps, the polar angle θ. The upper left inset shows an expanded view of electron trajectories at the MCP, demonstrating the VMI focusing conditions achieved with the 13-electrode design. At 5 eV, the SIMION results for our 13-electrode spectrometer indicate a ΔE/E of 0.85%, compared with 1.3% in our simulation of the standard 3-plate VMI design. The 13-electrode design also shows significantly reduced chromatic aberration relative to the standard 3-plate VMI. We emphasize that our design is not restricted to 3D VMI measurements; the fields can easily be configured for 2D VMI, with performance comparable to that of a dedicated 2D instrument[33].

Our SIMION results show that, for 5 eV photoelectrons, our 13-electrode design has a TTS of Δt = 8.6 ns while maintaining VMI focusing conditions. We note that the analogous standard 3-plate VMI would have a TTS of 1.8 ns. Given that the electron TOF resolution is limited, an increased TTS results in improved z-coordinate resolution (corresponding to the polar angle θ of the photoelectron distribution). Furthermore, for typical MCP detectors, the output electron pulse duration is on the order of 2 ns FWHM, suggesting a pulse-pair resolution (the minimum resolvable time difference between two pulses) of roughly half of this value. We note, however, that deconvolution using the instrumental single-hit time response function can lead to improved single-pulse and pulse-pair resolution (vide infra). Most importantly, an extended TTS allows for the detection and time-stamping of several electron events per laser shot.

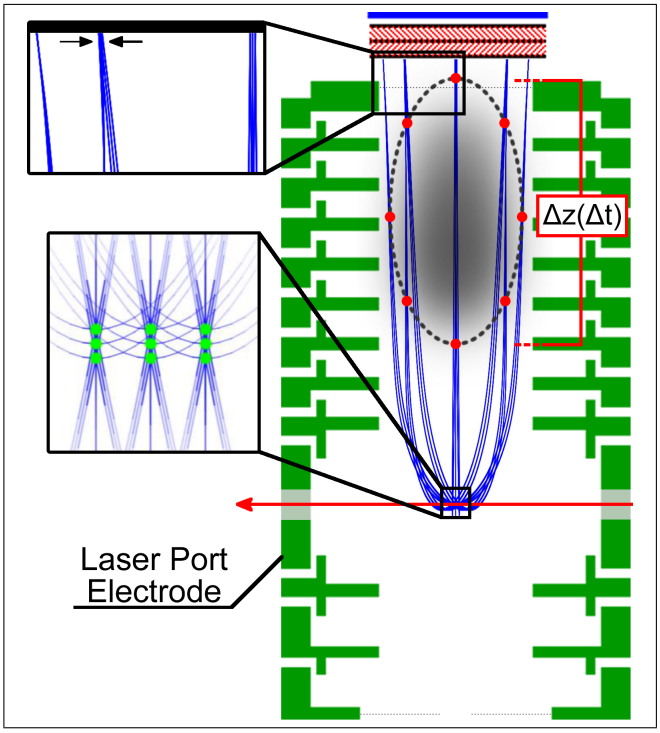

FIG. 2. Expanded view of the 13-electrode 3D VMI spectrometer design. Simulated electron trajectories (blue) with examples of time stamps (red dots) are shown to visualize the elongated photoelectron distribution Δz corresponding to a time-of-flight spread Δt. The upper inset shows a close-up of electron trajectories at the MCP detector, demonstrating that VMI focusing conditions are retained with the 13-electrode design. The lower inset shows the origins (green dots) of the simulated trajectories (for details, see the text). Note that the cross section depicts the laser axis (red) passing through the laser port electrode; the segments directly above and below the laser axis together comprise this single electrode.

3D VMI Electrode Stack

As shown in Figs. 1 and 2, the laser axis passes through a (large) 2 cm diameter hole in the laser port electrode, thus minimizing scattered UV light which can produce background photoelectrons from metal surfaces. A set of optical baffles helps to reduce the UV scatter. The 40 mm diameter MCP is mounted at a distance of 125 mm from the laser axis. Above the laser port electrode sits a stack of eight electrodes followed by the top (mesh-covered) electrode defining the end of the TOF region. Finally, a flat-field electron acceleration or deceleration region before the MCP permits optimally efficient photoelectron detection. These eight lens electrodes are 3 mm thick at their inner edges and have an internal aperture diameter of 50 mm. The electrodes just above and below the thicker laser port electrode are separated by 44 mm. The distance from the (mesh-covered) bottom electrode to the laser axis is 54 mm.

The top and bottom electrodes are made from CuBe in order to match their thermal expansion coefficients with that of the attached OFHC copper meshes. All other electrodes, the mesh electrode holders, and the lens mounting assembly are manufactured from minimally-magnetic and chemical-reaction-resistant 316 stainless steel. The bottom electrode is covered by a flat, gold-plated electroformed copper mesh which has a laser-machined 3 mm diameter central hole for skimmed molecular beam transmission. The molecular beam was veri-

fied to pass through the mesh without interference, as confirmed by the observation of cold clusters in the interaction region. The top electrode is covered by a 92% transmission gold-plated copper mesh. These meshes are gold-plated for electrical uniformity and chemical inertness, as well as to increase their work functions. The voltage varies linearly from the first electrode above the laser port to the top electrode, with the latter set to ensure that the electrons transmitted though the top grid are accelerated to 300-500 eV for maximum detection efficiency by the MCP. The three electrodes below the laser port serve to mimic a flat repeller plate while simultaneously displacing the bottom grid from the laser axis, thus reducing spurious electron generation by scattered UV light. The TOF tube is enclosed by single-layer mu-metal magnetic shielding, reducing external magnetic fields by a factor of 1000.

3D Electron VMI Apparatus & Data Acquisition Procedures

As depicted in Fig. 3, the skimmed molecular beam was directed along the TOF (z) axis. Our molecular beam source consisted of a 1 kHz Even-Lavie[34] pulsed supersonic valve (PSV) mounted inside a source vacuum chamber pumped by a large turbo-pump and skimmed by a Beam Dynamics, Model 1A, 1 mm skimmer. The duration of the gas pulses was less than 20 μs. The VMI electrodes shown in Figs. 1 and 2 were removed from Fig. 3 for clarity. The chevron dual plate MCP assembly incorporated a P47 phosphor screen anode (Photonis APD 2 PS 40/12/10/8 I 60:1 EDR P47). The phosphor emissions were imaged by a 25 GigE CMOS camera (Emergent Vision Technologies, HB-2800-S-M) capable of continuous streaming at 1 kHz with a 512×512 pixel resolution. Each electron event on the MCP anode was also decoupled through a 100 pF pickoff capacitor, propagated along an in vacuo SMA cable and doubled-ended SMA feedthrough, amplified (10× gain, 300 MHz analog bandwidth) and recorded by a 12-bit 4 GS/s digitizer card (AlazarTech, ATS9373). These waveforms were transferred in real time to a data acquisition computer, where post-processing (vide infra) determined the precise arrival time and amplitude (i.e. total charge) of each hit.

The choice of camera necessitated careful consideration. Specifically, we required a camera capable of running continuously at 1 kHz (the pulse repetition rate of our laser systems) with primary concerns being the low-light sensitivity and noise characteristics of the sensor. These in turn determine the percentage of total electron events which can be detected above the background noise. Camera sensitivity is often characterized by the quantum efficiency (QE), the percentage of incoming photons which are converted to electrons by the sensor. The QE is a wavelength-dependent parameter: we considered sensors with high QE near 400 nm (the central emission wavelength of the P47 phosphor). A useful measure of the low light performance of a camera sensor is given by the Absolute Sensitivity Threshold (AST) as defined in the EMVA1288 standard[35]. The AST is the mean number of photons which result in a signal-to-noise ratio of unity. As such, it combines the sensitivity and noise characteristics to give a measure of the minimum detectable signal. Combined with the requirement for high transfer speed, this led us to consider the 25 GigE (Giga-bit Ethernet) based cameras from Emergent Vision Technologies (EVT) which use the Sony Pregius (IMX) series of CMOS sensors. As mentioned above, our final choice was the EVT HB-2800-S-M camera which uses the Sony IMX421 CMOS sensor. It should be noted that even with the high sensitivity afforded by the IMX421 sensor, we are still operating at the low end of the camera's dynamic range. That is, with our MCP detector, a single hit on the sensor will typically register a peak (single pixel) value of less than 10 on an 8-bit (0-255) ADC. However, this is not a major impediment due to a combination of low readout noise and our ability to make use of the integrated full width of the single hit image spot (typically about 10 pixels FWHM). This allows us to accurately determine the position and amplitude (i.e. total charge) of single electron hits, as detailed below.

The event timing and data acquisition electronics used with our femtosecond and picosecond photoionization lasers is presented schematically in Fig. 3. The master clock of one of our laser systems generates a continuous 1 kHz pulse train which triggers four digital delays. The kHz PSV is pre-triggered by Delay 1. The switch-out Pockels cell is triggered by Delay 2, producing the output laser pulse from a regenerative amplifier. Delays 3 and 4 trigger the GHz digitizer and CMOS camera, respectively. The delays for the camera and digitizer are gated by the data acquisition computer so that they may only be triggered while collecting data. We will refer to the associated gate-closed state as Standby mode and the gate-open state as Acquisition mode. For stable operation, it is necessary to run both the PSV and laser continuously at 1 kHz, even in Standby mode. During Acquisition mode, we collected camera images and digitized waveforms in gated sets of laser shots (typically 4000). We then switched back to Standby mode for block data transfer. The depicted kHz Waveform Stack (blue) and kHz Image Stack (green) illustrate this block transfer. Acquisition of 4000 laser shots took 11 seconds including data transfer time, giving a duty cycle of 36% for the experiments presented here. However, recent improvements in data acquisition have increased the duty cycle to greater than 90%.

The kHz Waveform Stack is saved to disk. However, writing the kHz Image Stack to disk is slow and inconvenient due to the large data volume. To reduce this to manageable levels, the images are processed in real time in order to identify features above a set threshold and only a 31×31 pixel Region of Interest (ROI) enclosing each feature is saved to disk. These saved ROIs are subsequently treated by more time-consuming post-processing in order to yield accurate 2D positions and amplitudes,

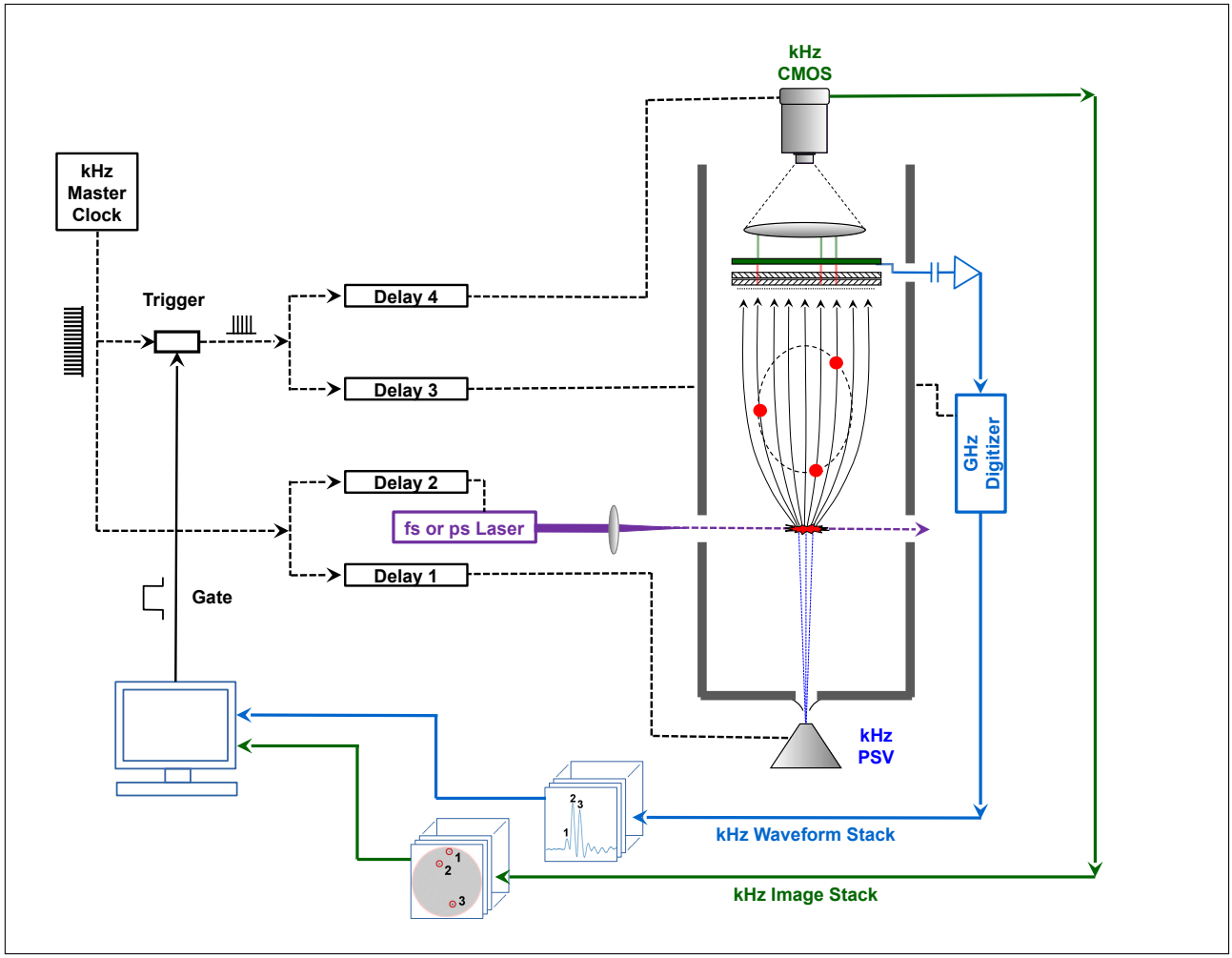

FIG. 3. Schematic diagram of the triggering and data acquisition setup used here. The 1 kHz Master Clocks of the implemented laser systems (upper left) provide the base trigger pulses used for these experiments. Triggers for individual devices (Delays 1-4) are timed by digital delay generators. During an experiment, triggering is switched between two different modes, Standby and Acquisition, as set by the status of a computer controlled Gate pulse. In Standby mode, the kHz pulse train passes only to Delay 1 and Delay 2, triggering the pulsed supersonic valve (PSV) and the switch-out Pockels cell of the femtosecond or picosecond laser, respectively. Running these continuously at 1 kHz is important for maintaining stability. In Acquisition mode, the kHz trigger also passes through to Delay 3 and Delay 4, triggering the GHz Digitizer and the kHz CMOS camera, respectively. For more accurate timing, the Digitizer may also be triggered by a photodiode signal from the laser pulse itself. The Digitizer records an amplified capacitive pickoff signal from a P47 phosphor screen anode on the MCP detector. Simultaneously, the CMOS camera images the correlated P47 emission. Data is collected in stacks of 4000 images and waveforms, upon which the system returns to Standby mode for block transfer of the data. The Waveform Stack is directly saved to a hard drive for post-processing. To greatly reduce the data volume, the Image Stack is pre-processed in real time to identify features corresponding to electron hits; only 31×31 pixel regions of interest around each hit are saved to disk.

as described below.

In order to test our 3D VMI spectrometer's capabilities, we used two separate laser systems for four different molecular beam photoionization experiments. For the first two experiments, a femtosecond kHz laser system generated 200 nm pulses for two-photon non-resonant photoionization of atomic xenon, producing 0.27 eV electrons. Our goal was to demonstrate our ability to properly time-stretch the photoelectron distribution and time-stamp the resulting electron events as an initial test of our equipment and methods. To evaluate the effectiveness of the time-stretching, we performed two such xenon experiments, one with a TTS of 8.8 ns (using a ~4.3 V/cm extraction field) and the other with a larger TTS of 31 ns (using a weaker ~1.6 V/cm extraction field). We used linearly polarized light along the x-axis (in the detector plane) to produce a cylindrically symmetric photoelectron distribution that could also be Abel inverted in order to provide a direct comparison with 2D VMI results. The gas mixture used for the 8.8 ns TTS xenon experiment was 2% xenon in helium at a stagnation pressure of 5 bar, and for the 31 ns TTS xenon experiment we used

5% xenon at a stagnation pressure of 2 bar.

The third experiment used the same femtosecond laser system as above to perform resonance-enhanced two-photon ionization of CH_3I with 200 nm pulses, producing 2.78 eV electrons. We used an extraction field of ~16 V/cm (non-optimal) and achieved a TTS of 6.9 ns. The goal of this experiment was to test our time-stretching and time-stamping ability with electron energies higher than in the xenon experiments. We used a gas mix of 2% CH_3I in helium at a stagnation pressure of 1 bar.

The femtosecond laser source for the xenon and CH_3I experiments (Coherent, Legend Elite Duo) produced 800 nm, ~40 fs pulses at a repetition rate of 1 kHz. We used ~0.7 mJ of the laser output to produce 200 nm pulses (fourth harmonic) by nonlinear frequency conversion methods.

For the final experiment, a 150 ps kHz Nd:YVO_4 laser system generated narrow band (i.e. transform-limited) pulses at 213 nm and 266 nm. These pulses were used to photodissociate the nitric oxide dimer $(NO)_2$, producing NO(A) state photoproducts, which were then photoionized[36]. The NO(A) state is long-lived (~100 ns) and has almost perfect Rydberg 3s character. Single-photon ionization of the NO(A) product with a 266 nm picosecond pulse therefore produces a very narrow 0.84 eV photoelectron kinetic energy distribution with almost perfect p_z-wave character (where z here is the 266 nm laser polarization axis). We used an extraction field of ~ 11 V/cm and this resulted in a TTS of 6.2 ns. For the NO dimer experiment, we used 20% NO in helium at a stagnation pressure of 5 bar.

The laser source for the NO dimer experiment was a home-built Nd:YVO_4 Grazing Incidence Slab Laser, seeded by a 150 ps Nd:YAG SESAM mode-locked oscillator (Time-Bandwidth Products), yielding amplified (~1 mJ) 1064.7 nm, 150 ps TL pulses at a repetition rate of 1 kHz. The $(NO)_2$ photodissociation laser pulse (212.94 nm, fifth harmonic) and the NO(A) probe laser pulse (266.18 nm, fourth harmonic) were produced using conventional nonlinear frequency conversion schemes. We note that, as a predominantly Rydberg s-orbital, there is no electronic angular momentum polarization of the NO(A) photofragment and therefore its Lab Frame photoelectron angular distribution is determined only by the probe laser polarization (defining the z-axis of the distribution) and the ionization dynamics (here, p_z-wave photoemission). Importantly, a 266 nm waveplate was used to freely rotate the linear polarization of the probe pulse relative to the 3D VMI TOF axis. This allowed us to generate p-wave photoelectron angular distributions peaked along the freely rotatable probe laser polarization direction, thereby providing stringent tests of our 3D VMI capabilities. The time delay between the 212.94 nm photodissociation and 266.18 nm probe pulses was 2.1 ns. This ensured that the second (photoionization) pulse arrived well after the first and the asymptotic photoproduct distribution had fully formed.

Our ability to interpret data containing multiple electron events per laser shot is contingent upon a correct determination of the 2D (x, y) position (from the CMOS camera image) and matching TOF (from the transient digitizer waveform) for each event in the shot. To accomplish this, we make use of the nature of MCP amplification as an avalanche process described by a gain PHD. Each single electron event will sample the broad PHD and the resulting total charge will be reflected in the integrated amplitudes of both the camera and digitizer signals. As an example, for a laser shot resulting in three electron events (as depicted in Fig. 1), the event that experiences the highest MCP gain will produce the highest amplitude pulse on the digitizer waveform and, concomitantly, the most intense spot on the camera image. Similar arguments apply for the next and lowest gain electron events. For this reason, 3D VMI benefits from an MCP with high gain but a broad PHD, the latter being considered undesirable in most event counting applications. The detailed analysis of these 3D VMI data and the associated characterization of this instrument are presented in the following sections.

III. DATA ANALYSIS

A 3D VMI data set consists of a stack of 2D camera images and a correlated stack of digitized GHz waveforms, wherein each image-waveform pair comprises the electron detection events for a single laser shot. For a given laser shot, each electron event (hereafter, a hit) on the MCP detector is recorded as both a phosphorescence spot in the 2D image and a short electrical pulse in the waveform. The image data contain the spatial (x, y) information for each hit, whereas the digitized waveform data contain the time information. We will refer to a hit in the image data as a position-hit (p-hit) and a hit in the waveform data as a time-hit (t-hit). The images and waveforms are first analyzed independently, determining the p-hit (x, y) and t-hit (time) coordinates and their associated amplitudes. The p-hit and t-hit amplitudes, both representing the same total charge sampling the MCP's gain PHD, are essential for matching the spatial and temporal coordinates for each hit.

Image and p-Hit Analysis

The camera images must be processed to determine the x and y position of each hit as well as its amplitude. As described above, the full 512×512 pixel images are not saved to disk. Rather, features above a set threshold are identified during collection and only 31×31 pixel regions of interest (ROIs) centered on each feature are saved. After data collection, these ROIs are later processed by subtracting the average background level and the average x and y projections, then smoothing using a 2D Gaussian filter (5 pixel FWHM). The x and y coor-

dinates are extracted by interpolating lineouts through the maximum along each axis and precisely fitting the peak positions. For the associated amplitude, we take the maximum value of the smoothed ROI. To illustrate this process, we consider a sample camera image from the aforementioned two-photon 200 nm atomic xenon ionisation experiments. This sample image is presented in Fig. 4, demonstrating the size and structure of typical p-hits. The image in Fig. 4 (a) is a 200×200 pixel region containing 2 p-hits, taken from a full 512×512 image. This is shown, rather than the single-hit ROIs used in the analysis, so that both p-hits can be viewed together. The lineouts through both p-hits along the y (Fig. 4 (b)) and x (Fig. 4 (c)) directions are also presented. It can be seen that the structure of both the p-hits and the noise is the same along both axes. The shape of a typical p-hit is, to good approximation, Gaussian along both axes (Fig. 4 (d) and (e)). We are able to achieve a sub-pixel resolution of 0.2 pixels in x and y hit position using this data processing routine.

Waveform and t-Hit Analysis

The signature of a single t-hit as seen in the recorded waveforms has a complex but highly stable pulse shape due to the effects of capacitive decoupling and imperfect high frequency impedance matching. Below, we illustrate this behaviour and our associated analysis using data from the aforementioned 31 ns TTS xenon ionization experiment.

By averaging millions of measured single-hit waveforms, we can obtain a single-hit instrument response function, as shown in Fig. 5 (a). We term this the Global Single-hit Response (GSR) since it represents a global average of single-hit waveforms including events sampling all spatial regions of the detector. However, a closer analysis of the same data shows that there is a small variation in the single-hit pulse shape which depends on the spatial location of hits on the detector. An important question therefore arises: with what accuracy can the GSR be used as a deconvolution kernel for the global analysis of multi-hit waveforms?

We therefore devised the following quantification of the GSR accuracy across the detector face. To facilitate comparison of these local variations with the GSR, we first prepared a set of Local Single-hit Response (LSR) functions representing an average of many single-hit waveforms with the constituent events for each being constrained to a different spatial region. Specifically, the LSRs were obtained by binning the spatial region of the detector into a 20×20 grid, as shown in Fig. 5 (c). Within each grid square, an LSR analogous to the GSR in Fig. 5 (a) was generated using only hits where the corresponding spatial position falls within that square.

We constructed an artificial, precisely known double-hit test trace, shown in Fig. 5 (b). This trace is a sum of three components: (i) the GSR with its peak at time **t1**; (ii) the GSR with its peak at time **t2**; and (iii) a sample of typical experimental noise taken from a representative waveform containing zero hits. This test trace was generated with a precise time difference ($\Delta t = \mathbf{t2} - \mathbf{t1}$) between the two GSRs of 10.00 ns, and a precise amplitude ratio ($A2/A1$) of 1.00 (i.e. the amplitudes of the GSRs at **t1** and **t2** were identical). We used this test trace to evaluate systematic errors in both Δt and $A2/A1$ as a function of the spatial location of the LSR. This was achieved by deconvolving the double-hit test waveform of Fig. 5 (b) using each individual LSR rather than the GSR, followed by Gaussian fitting to obtain the time and amplitude of each hit. The Δt and $A2/A1$ values extracted by using the LSRs can then be compared with their precisely known values, yielding a 2D spatial map of these systematic errors, as described below. Note that a double-hit rather than a single-hit test trace was used here because Δt and $A2/A1$ are independent of any uniform time offset (e.g. trigger jitter) or amplitude variation (i.e. the PHD).

The spatial variation of the extracted values of Δt and $A2/A1$ are presented on a grid representing the same spatial bins used to determine the LSRs. The range of the variation in Δt (Fig. 5 (d)) can be seen to be about 40 ps, which we consider to be acceptable and negligible on the basis that it is significantly less than our experimental time resolution (see below). The amplitude ratios $A2/A1$ obtained using different LSRs are similarly shown in Fig. 5 (e), where it can be seen that the scale of the variation is about 5% over most of the detector, which we judge to be small enough to neglect. From this analysis, we conclude that we are justified in using the GSR as a global deconvolution kernel in our subsequent analysis.

Deconvolving our raw waveform data with the GSR removes the complex instrument response function (Fig. 6 (a)) from the traces prior to peak picking, as shown in Fig. 6 (b), where the deconvolved waveform (orange) more clearly shows a single hit. Furthermore, deconvolution enhances our resolution of individual hits in a multi-hit waveform, as demonstrated by Fig. 6 (c), where it can be seen that the three hits in this exemplary multi-hit trace are clearly resolved after deconvolution. We note that the amplitudes of the two highest peaks after deconvolution (the true amplitudes) are nearly identical, whereas the amplitudes appear to be different in the raw data due to the single-hit pulses being overlapped in time.

The deconvolved traces shown in Fig. 6 and those used in our data analysis were all smoothed with a 0.3 ns Gaussian filter prior to peak picking. The width of this filter was chosen as a compromise between signal-to-noise ratio and time/amplitude resolution. Peak-picking following deconvolution is accomplished in two steps. For each trace, we first identify all local maxima above a set threshold. A region surrounding each maximum is then fit to a Gaussian function, yielding the peak position and amplitude. For cases with N overlapping local maxima, the region surrounding this set of maxima is fit to a sum of N Gaussian functions, yielding a position and ampli-

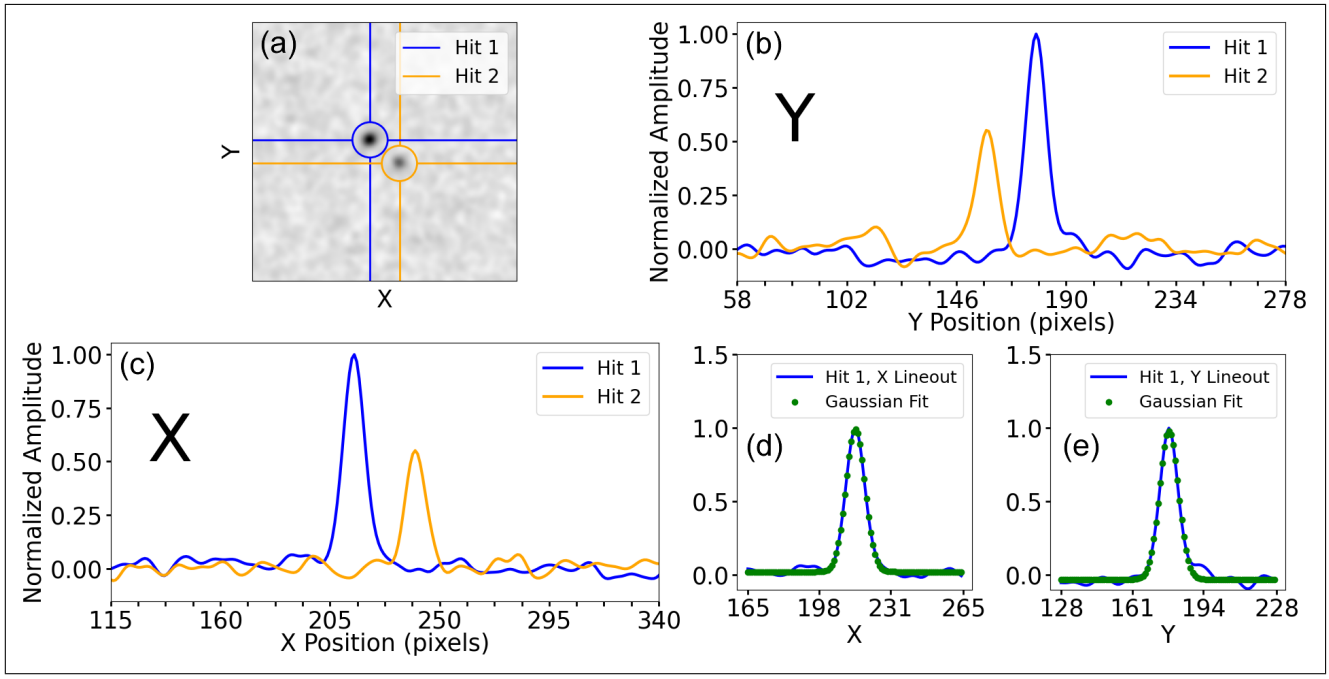

FIG. 4. Analysis of a sample experimental camera image. (a) A 200×200 pixel region taken from a full 512×512 pixel image. This image has been processed as described in the main body of the text. Two hits of different heights are visible, marked by the vertical and horizontal lines. A typical hit has a FWHM of about 10 pixels along each axis. (b-c) Lineouts through both hits (blue, Hit 1, and yellow, Hit 2) along the y-axis (b) and x-axis (c) showing their relative height compared to the experimental noise. The pulse shape and noise characteristics are the same along each axis. (d-e) A zoom-in of the x (d) and y (e) lineouts (blue) through hit 1, with Gaussian fits (green) to each.

tude for each.

Our single-hit time resolution, averaged across the 40 mm diameter MCP, was determined by detecting scattered single UV photon hits from the femtosecond laser. The measured variance of the apparent arrival times of the UV photons is due to the triggering jitter of the electronics combined with propagation effects on the MCP anode. This is therefore a measure of the TOF resolution for photoelectron signals. The distribution of photon arrival times was represented by a Gaussian function with a FWHM of 160 ps and we take this to be our global electron TOF resolution. We note that by co-adding an accurately timed laser pulse photodiode signal to the photoelectron TOF waveform, the electronic timing jitter can be largely removed. In this case, we expect the TOF resolution for a single hit to be considerably improved. We estimate that our minimum pulse-pair resolution (using a criterion of a 5% dip between peaks) is 0.4 ns for the favourable case of two hits of identical amplitude near the average amplitude of the data set. This minimum pulse-pair resolution can only be achieved by applying less smoothing to the deconvolved traces, resulting in a lower signal-to-noise ratio. For the data shown in Fig. 6, a higher level of smoothing was used, leading to a pulse-pair resolution of 0.75 ns.

Assigning Multi-Hit Data

Generally, our data sets contain multiple electron hits per laser shot. In order to make use of this multi-hit data, we must determine the best way of grouping the p-hits and t-hits from each laser shot into correlated pairs (one p-hit and one t-hit) so that the members of each pair can be confidently assigned to the same event. In the following, a pair will refer to a set of one p-hit and one t-hit, whereas an assignment will refer to a set of pairs belonging to the same laser shot. Assigning the multi-hit data is accomplished by making use of the fact that each event is randomly subjected to a different gain when amplified by the MCP, as described by the MCP's PHD. Thus, the more intense hit of each type (p and t) are likely to form a correctly matched pair, as are the next most intense hits of each type and so on. However, this is not so simple in practice, since the measured amplitude of each hit is subject to instrument noise, which is different for the camera (p-hit) and digitizer (t-hit). This leads to some variation in the ratio of the p-hit and t-hit amplitudes associated with the same event, despite the equivalent MCP gain. As such, it is often ambiguous which hits form a correctly matched pair, specifically when there are multiple reasonable ways of assigning the hits from one laser shot.

There are also many shots in which the number of p-hits and t-hits are not equal. This can occur if a hit

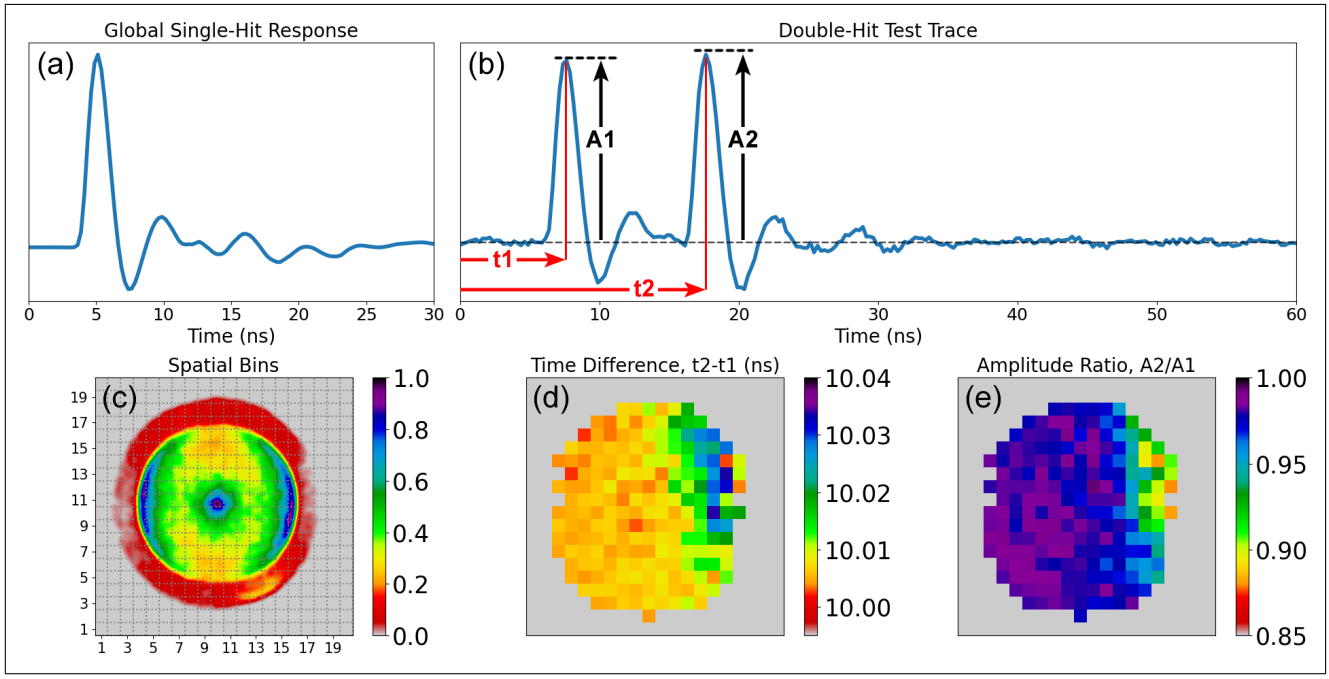

FIG. 5. Demonstration of the validity of the Global Single-hit Response (GSR) as a deconvolution kernel for extracting time-of-flight and amplitude information in a 3D VMI experiment. The experimental data set used in this analysis is the 31 ns TTS 2-photon ionization of xenon at 200 nm, as discussed in the text. (a) The GSR waveform, to be used as a deconvolution kernel, which is an average of many single-hit waveforms sampled across all spatial regions of the MCP detector. The structure of the GSR pulse is highly stable over time and specific to our instrument. (b) An artificial double-hit test trace constructed to quantify systematic errors. It is the linear superposition of three components: the GSR at time $t1$, the GSR at time $t2$, and an experimental trace containing zero hits (i.e. experimental noise). The value of $\Delta t = t2 - t1$ was set to 10.00 ns and the ratio of peak amplitudes $A2/A1$ was set to 1.00. (c) The spatial distribution of all hits from the experimental 31 ns TTS xenon data set with the colour representing hit density. The sharp cutoff indicates the edge of the MCP detector. The grid lines and axis labels indicate the spatial binning of the data into a 20×20 grid. A localized average pulse shape similar to (a) was constructed for each bin using only hits within that bin and each of these were used as a kernel to deconvolve the test trace in (b). (d-e) Spatial maps of the time difference Δt (d) and amplitude ratio $A2/A1$ (e) obtained by using localized kernels from the corresponding bins in (c) to deconvolve the test trace (b) followed by curve fitting.

results in a gain on the lower end of the MCP's PHD and the signal falls below the noise level on one instrument but not the other. Since the camera images have a lower signal-to-noise ratio than the digitizer, this is most likely to result in t-hits without a matching p-hit, rather than the converse. There are also many cases where two or more pulses on the waveform overlap and the t-hits cannot be resolved, thus appearing as a single pulse. This results in the opposite effect: one or more p-hits appear without matching t-hits. This effect will also be seen if hits resulting from laser scatter arrive outside the time window of the digitizer but are still captured in the camera image. We note that the effect of pulse overlap is mitigated by the application of time-stretching, since the same pulses arrive within a wider time window and are therefore easier to resolve. The effectiveness of time-stretching on our ability to correctly assign multi-hit data is demonstrated in Section IV.

It is possible to discard any shots which have ambiguous assignments or unequal numbers of p-hits and t-hits, but this would mean discarding a large amount of potentially usable data. Even if it is not feasible to confidently assign all of the hits in a multi-hit laser shot, it is still possible to make use of a substantial fraction of them. In order to quantify the level of agreement between the correlated amplitudes of a pair, and thus properly compare multiple possible assignments, it is necessary to develop a better understanding of the amplitude distribution of correctly matched data. This distribution is represented as a plot of t-hit amplitude versus p-hit amplitude for single-hit data, as shown in Fig. 7 (a). Since this characterization is a prerequisite of the multi-hit treatment, it is necessary to consider only single-hit data for which it can be assumed that the p-hit and t-hit belong to the same event. We will refer to this Single-Hit Amplitude Distribution as the SHAD in the following.

For multi-hit data, the likelihood that a pair is correctly assigned (that is, that the p-hit and t-hit belong to the same event) depends on the degree to which the amplitudes of the pair agree with the SHAD. For this reason, it is important that the SHAD is as narrow as possible so that pairs can be confidently assigned. The SHAD associated with the aforementioned 8.8 ns TTS xenon data is shown in Fig. 7 (a). This SHAD (as well as

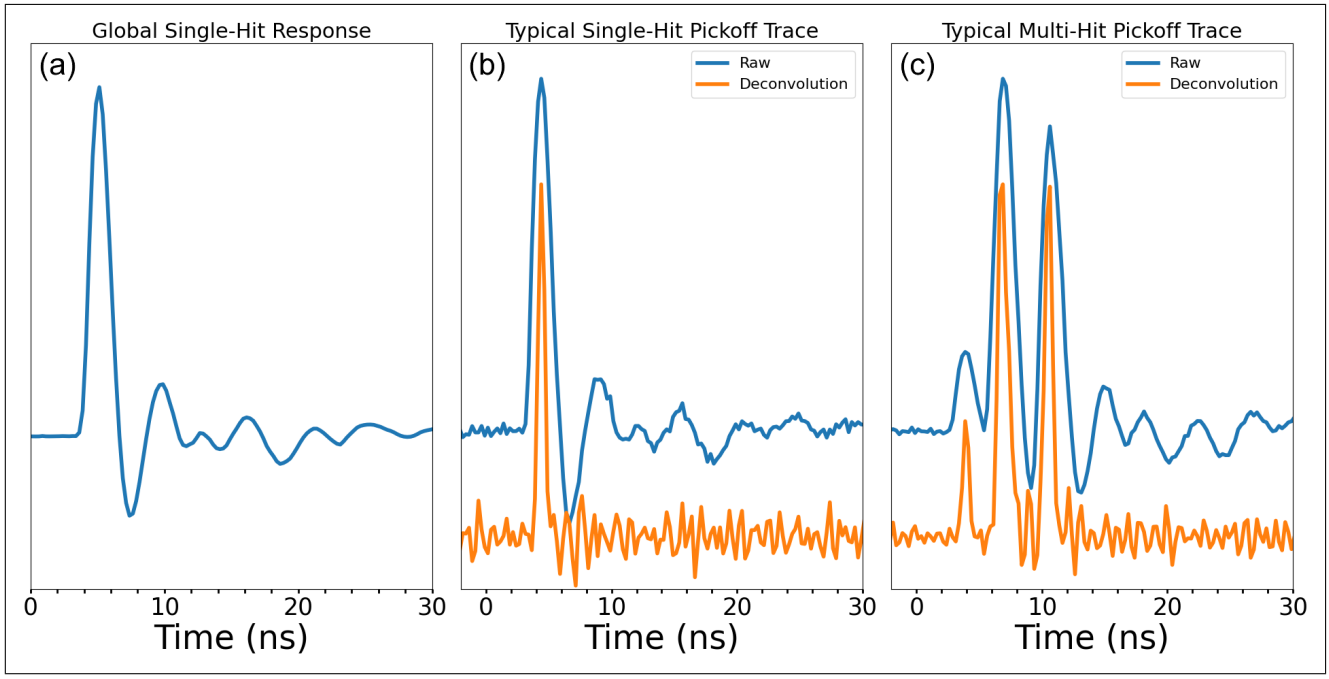

FIG. 6. Deconvolution of typical single-hit and multi-hit traces using the average single-hit pulse shape as a kernel. (a) The deconvolution kernel obtained by averaging many single-hit traces. (b) Deconvolution of a sample experimental single-hit trace using the kernel shown in (a). (c) Deconvolution of a sample experimental multi-hit trace using the kernel shown in (a). Both deconvolved traces have been smoothed using a 0.3 ns Gaussian filter.

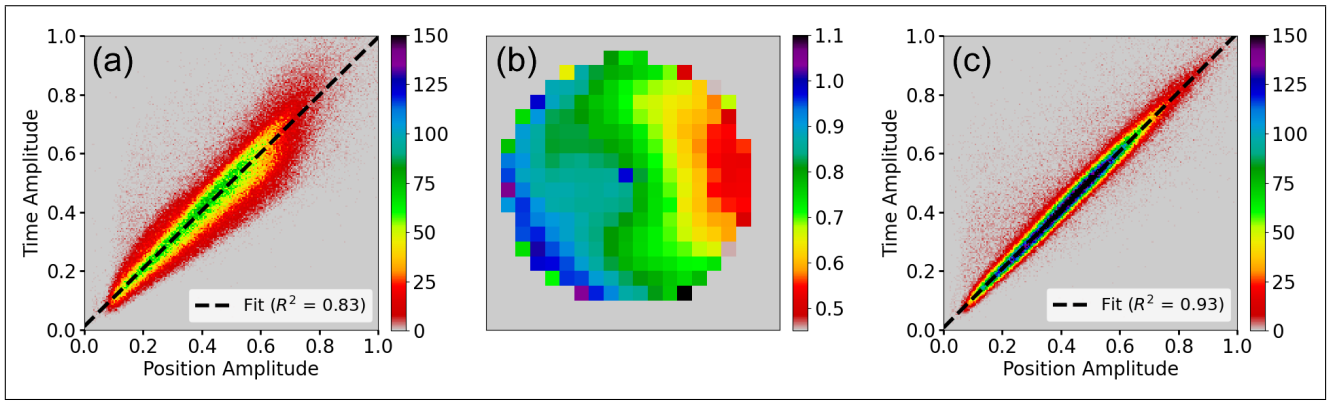

FIG. 7. The Single-Hit Amplitude Distribution (SHAD) from the 8.8 ns TTS xenon experiment described in the text, before (a) and after (c) correction for the spatial variation (b) of the time and position amplitude correlation across the phosphor screen of the detector. The SHAD shows the distribution of correlated position (from the camera image) and time (from the capacitive pickoff) amplitudes using only single-hit data. It is necessary to use single-hit data since it can be assumed that in the single-hit case, the hits from each detector source (1 position and 1 time) correspond to the same event. For multi-hit data, the position-time pairings are made with reference to the SHAD as described in the text. (b) The spatial region imaged by the camera, divided into a 20×20 grid. The single-hit data are binned according to where they fall within this grid. The color represents the slope of the SHAD, using only hits from each bin, and the sharp cutoff indicates the edge of the MCP detector. We observe that the slope of the SHAD exhibits a clear gradient from the upper-right to the lower-left of the detector. (c) To correct for the spatial variation of the slope, we scale the amplitude of the position data so that the average slope in each bin is 1. This results in a more narrow distribution which allows us to better pair time and position hits in multi-hit data.

the qualitatively similar SHADs of the other data sets) is fairly broad, which impedes its use in assigning multi-hit data. One of the reasons for this is that the amplitudes of the p-hits vary significantly depending on the spatial location of the p-hit on the detector. Since the t-hits do not display the same spatial variation, this cannot be a result of a spatially dependent MCP gain (which would affect the t-hit and p-hit amplitudes equally) but is rather most likely caused by spatial variation in the phosphor efficiency. A spatially dependent phosphor efficiency could

be a result of manufacturing imperfections in the phosphor screen and/or due to experimentally-induced degradation of the phosphor. This spatial variation manifests as a broadening of the SHAD as a result of its spatially dependent slope.

We correct for the spatial variation of the SHAD by first binning the single-hit data into an equally spaced 20×20 grid based on the location of the p-hit on the detector. This is presented in Fig. 7 (b), where the value assigned to each square is the slope of the SHAD using only hits within the corresponding spatial bin. We use a 20×20 grid since it is both fine enough to show the structure of the spatial variation of the slope as well as coarse enough so that each bin has a large enough sample size to give a sufficiently accurate value for the slope. For the ~200,000 single-hit shots in the 8.8 ns TTS xenon data set, this grid size results in bins containing 100 to 5000 hits. Fig. 7 (b) highlights a clear gradient in slope from the upper-right to the lower-left of the detector. To correct the data, we scale the p-hit amplitudes in each bin by the slope of the SHAD associated with that bin. This ensures that the average slope in each bin will be 1. After correction, the SHAD is narrowed significantly, as shown in Fig. 7 (c).

For a general laser shot with N p-hits and M t-hits, there are $N * M$ possible pairs that can be formed. To determine the best assignment (the set of pairs which are most likely to be correctly matched), we must quantify the degree to which each pair agrees with the SHAD. This value, which we will call the quality of the pair, is assigned by evaluating the smoothed SHAD at the point corresponding to the amplitudes of the pair. Since the SHAD is the observed density of single hits as a function of their amplitudes, its value at a certain amplitude pair represents the likelihood of observing that pair. This assumes that the hits in a multi-hit shot can be considered independent events, which we accept since the hits typically occur in different spatial regions of the detector and should not interact. We represent the qualities of the $N * M$ possible pairs as an $N * M$ matrix which we will call the quality matrix Q.

The rows and columns of the Q matrix represent pairs which contain the same p-hit (rows) or t-hit (columns), so accepting one pair as part of an assignment will necessarily involve rejecting all other pairs in the same row and column. Consequently, it is better to evaluate the quality of a multi-hit assignment as a whole rather than the individual pairs that belong to it. We will define the quality of an assignment as the product of the qualities of the pairs it contains. Since the quality value for a pair represents the likelihood of observing that pair, the product of the qualities of pairs belonging to an assignment will represent the likelihood of observing that assignment. To make the most probable assignment, a set of all possible n-pair assignments is constructed, where n is the minimum dimension of the Q matrix. The best assignment is then the one with the greatest quality. In our current analysis, this assignment is accepted without further consideration. However, we are currently developing a Bayesian inference method for comparing pair assignments having similar quality values, in order to evaluate when all or part of a multi-hit assignment should be rejected on the basis of statistical ambiguity. This will be presented in a future publication.

One way to quantify the efficiency of the multi-hit data analysis described above is by the average number of correctly assigned hits per laser shot. Since we are primarily concerned with characterizing our ability to handle higher hit-count data, it is instructive to consider how the number of correctly assigned hits varies with the total number of hits in the shot. In Fig. 8, we present this information for each of the four experiments described above (31 ns TTS Xe, 8.8 ns TTS Xe, 6.9 ns TTS CH_3I, and 6.2 ns TTS NO). Note that the distribution of hit counts was lower for some of the experiments (8.8 ns TTS Xe and 6.2 ns TTS NO) so the higher hit counts are not well represented in these data sets. In Fig. 8, the dashed line represents the maximum possible efficiency, where the number of correctly assigned hits is exactly equal to the total hit count. The number of hits in an experimental laser shot can be ambiguous when there are unequal numbers of p-hits and t-hits. For grouping the data by hit count to produce Fig. 8, we used the number of p-hits to define the number of hits in the shot. This is a more reliable value than the number of t-hits since many waveforms suffer from unresolved time overlap of peaks, as mentioned above.

It is clear from Fig. 8 that the multi-hit assignment efficiency increases with the time spread of the photoelectron distribution. This trend is present even when considering photoelectrons of different kinetic energy (0.27 eV for Xe, 0.84 eV for NO, and 2.78 eV for CH_3I). We can correctly assign up to ~6 hits per shot for the case of the 31 ns TTS xenon experiment, and up to ~4 hits per shot for the higher-energy CH_3I case. Importantly, we have not seen a substantial drop in pair assignment (matching) efficiency with higher hit count, up to 15 hits per shot (the highest hit count we sampled). There are two major limiting factors for matching efficiency. The first is the ability to resolve individual t-hits, especially when the hit count is high. It is this factor which is addressed by the application of time-stretching, as is evident in Fig. 8. The other factor is the inability to resolve the difference in amplitude between hits. This issue can be addressed by using a high-gain MCP detector with a broader PHD, and we are currently developing modified MCP geometries as a method for improving this aspect.

It should be noted that not all of the hits that are assigned will be assigned correctly. In preparing Fig. 8, which shows only the correctly assigned hits, we also had to estimate the number of hits that were assigned incorrectly. This was achieved by constructing a pseudo-artificial data set, for which the correct assignments are known, corresponding to each of the experimental data sets. To create these pseudo-artificial data sets, previously processed and confidently assigned single hit am-

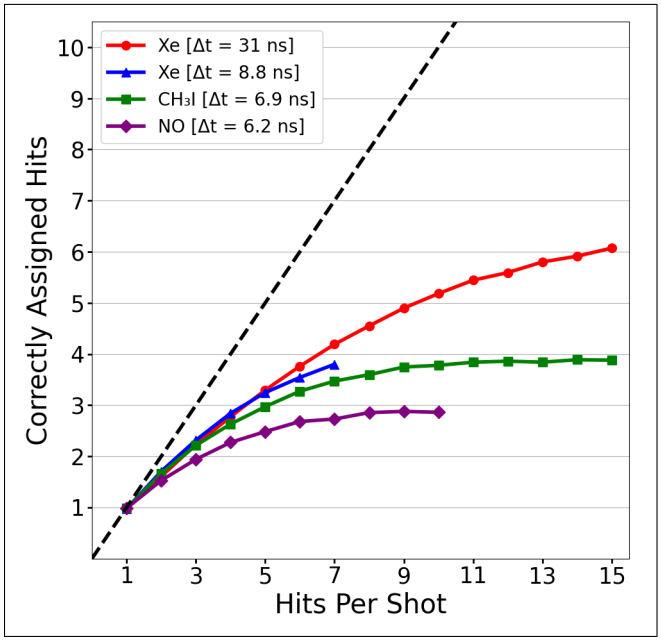

FIG. 8. The efficiency with which we can correctly extract and assign matching position (p-hit) and time (t-hit) coordinates in multi-hit 3D VMI data. Four different experiments using photoelectron distributions with varying kinetic energies are shown, with hit counts up to 15 hits/shot (except for the 8.8 ns xenon and 6.2 ns NO experiments where the hit count was lower). The process for assigning the data and estimating the number of correctly assigned hits is described in detail in the text. The dashed line represents the maximum possible efficiency (i.e. all hits in the shot are correctly assigned). These results show that a longer time spread results in a greater efficiency, and for the case of the 31 ns xenon experiment we can correctly assign up to 6 hits/shot. The 8.8 ns xenon, 6.9 ns CH_3I, and 6.2 ns NO experiments permitted correct assignments of up to 4, 4, and 3 hits/shot, respectively. These data were collected using the acquisition conditions described in Section II.

plitude pairs from the corresponding experimental data were randomly sampled and grouped into sets of 1-15 to form shots. These were analysed in an identical way to the experimental data, as described above, and the resulting assignments were compared to the known correct assignments. The ratio of correct to incorrect assignments was then applied to the experimental results to produce the data presented in Fig. 8. Incorrect assignments, where the position and time each belong to different events, will contribute a background signal distributed over the cylinder defined by the spatial and temporal coordinates sampled in the data set.

IV. RESULTS AND DISCUSSION

As discussed above, we performed a set of four experiments to test our 3D VMI apparatus and data acquisition. In particular, our goals were to demonstrate the following: the benefits of time-stretching on our multi-hit data handling capability; our ability to make use of high hit-count (>3 hits/shot) data; and the ability to perform VMI experiments with arbitrary polarization geometries (i.e. without the need for Abel inversion). The first two points were addressed in the previous section and demonstrated in Fig. 8. Here we will discuss the details of the four data sets that were collected, and address the final point (3D imaging without polarization constraints) using an $(NO)_2$ photodissociation and photofragment ionisation experiment.

For the xenon and CH_3I experiments, we collected image and waveform data for 800,000 laser shots (200 stacks of 4000 shots each). This corresponds to about 13.3 minutes of real-time data at a laser pulse rate of 1 kHz. However, due to the data transfer overhead between each stack of 4000 shots, the actual data collection time was about 37 minutes. As mentioned above, we have greatly reduced this overhead with recent improvements. For the NO dimer experiment, three data sets were collected at three different polarization conditions. Each of these consisted of 200,000 laser shots (50 stacks of 4000 shots each), corresponding to approximately 9 minutes of data collection time.

For each of the experiments, we present the resulting photoelectron distribution in the form of x-y slices along the z (TOF) axis (Figs. 9, 10, 11, and 12). The slices in these figures are not constructed from the image data directly. Rather, they are made by binning the processed 3D (x, y, t) coordinate data by arrival time and plotting the (x, y) positions within each time bin as a 2D histogram. Note that with the full 3D coordinates available, we also have the ability to produce 2D slices in the x-t, y-t, or any other arbitrary plane. In each case, the time width of the slices is equal to our time resolution of 160 ps. The slices shown here are primarily for visualization purposes and have been smoothed to enhance their qualitative features. As such, the rings associated with specific electron kinetic energy features are artificially broadened and their width does not reflect our actual energy resolution. The rings all appear to be highly circular as expected for a VMI image, with the small exception of the 31 ns xenon data set, as described below. Since the time spread of these experiments is much longer than the width of the slices, we can produce many more slices than the few shown in the figures presented here. The full time-binned data sets for two of the experiments (8.8 ns TTS xenon and NO dimer at 45° probe laser polarization) have been animated as videos and are available as supplementary material.

Figs. 9-12 also include histograms of photoelectron yield over time and each of these show a significantly higher background level at the back end of the distribution compared to the front end. This background signal is caused by photoelectrons produced from scattered light hitting the inner walls of the electrostatic lens system and is challenging to remove[37] when using UV light, where the photon energies exceed the work functions of

the electrostatic lens components.

Xe($^1S_0$) Photoelectron Imaging

The first test case for our 3D VMI apparatus and data processing was the 2-photon ionization of xenon at 200 nm:

$$\mathrm{Xe}\, 5p^6(^1S_0) + 2h\nu \rightarrow \mathrm{Xe}^+\, 5p^5(^2P_{3/2}) + e^-. \qquad (1)$$

As discussed above, we performed two experiments using this photoionization process, with the only difference being the implemented electrostatic lens voltages and the resulting degree of electron-distribution time-stretching (8.8 ns and 31 ns). These experiments allowed us to directly compare the effects of time spread on our results and analysis efficiency.

In these experiments, we only see ionization into the lower ($^2P_{3/2}$) of the two spin-orbit states of the ion[38], since two photons of 200 nm (12.40 eV) is less than the $^2P_{1/2}$ excited spin-orbit state ionization energy of xenon (13.44 eV). The ionization energy of xenon to the $^2P_{3/2}$ state is 12.13 eV and this results in a low, dominant photoelectron kinetic energy of 0.27 eV. We used a linear laser polarization perpendicular to the TOF axis in these measurements, which is the polarization condition necessary for performing conventional 2D VMI using Abel inversion. The average hit count was 1.0 and 8.7 hits/shot for the 8.8 ns and 31 ns experiments, respectively.

The analysed and time-stamped xenon data are presented in Fig. 9 (8.8 ns TTS experiment) and Fig. 10 (31 ns TTS experiment) in the form of slices through the 3D photoelectron distribution where the processed (x, y, t) data are binned by their arrival time. The TTS for each can be seen in the photoelectron yield over time, as shown in Fig. 9 (a) and Fig. 10 (a). For these experiments, the linear light polarization (x) axis is aligned in the vertical direction, which can be seen in the photoelectron distribution (most visible in panels (d) and (e) of each figure) where there is slight visible anisotropy with higher photoelectron intensity along the ± x-axis.

Our SIMION simulations predict that with optimized electrode settings we would expect a TTS greater than 40 ns for this xenon photoionization process. However, when we attempted such an experiment, we found that stretching beyond 31 ns produced significant distortions in the shape of the photoelectron distribution. This manifested primarily as a loss of circular symmetry in the electron rings, which became more square in shape. This effect was most severe for the later-arriving electrons, which spend more time in the extraction region of the VMI spectrometer. The distortions are also present, albeit to lesser degree, in the 31 ns results (Fig. 10). We believe that the cause of this loss of circular symmetry is due to the entrance and exit apertures in the laser port electrode. This is supported by the direction of the corners of the distortion, which line up with these ports. Furthermore, the severity of the distortion increases with the degree of time stretching; as the electron-projection field gradient is reduced to allow the slow electron distribution to expand along the TOF axis and detector face, the electrons move more slowly through the electrostatic lens, come closer to the laser port electrode, and are more susceptible to stray and inhomogeneous fields in the instrument. Thus, these trajectories are more sensitive to the presence of the electrode openings. We note that such electron distribution distortions are absent in higher electron kinetic energy data, such as that presented in Figs. 11 and 12, for which the instrument was designed. We plan to address this low-electron-kinetic-energy issue in the next version of our 3D VMI spectrometer, which is currently under construction.

CH_3I Photoelectron Imaging

Here we present a second test system which allows us to demonstrate the 3D imaging of higher-energy photoelectrons. For this, we used two-photon ionization of CH_3I at 200 nm[39], which results in 2.78 eV electrons:

$$\mathrm{CH_3I}\,(\mathrm{X}\,^1A_1) + 2h\nu \rightarrow \mathrm{CH_3I^+}\,(\mathrm{X}\,^2E_{3/2}) + e^-. \qquad (2)$$

Here, we were able to achieve a time spread of 6.9 ns. As with the xenon experiments, we used a linear laser polarization perpendicular to the TOF axis, allowing us to also perform an inversion-based analysis of the data. The average hit count of this data set was 3.2 hits/shot.

The analysed and time-stamped CH_3I data are presented in Fig. 11 in the form of slices through the 3D photoelectron distribution. The 6.9 ns TTS can be seen in the photoelectron yield over time (Fig. 11 (a)). The linear light polarization (x) axis is aligned in the vertical direction, as evidenced by the clear anisotropy in the photoelectron distribution (Fig 11 (b-h)) with higher photoelectron intensity along the ± y-axis.

NO($\mathrm{A}\,^2\Sigma^+$) Photoelectron Imaging

As a powerful demonstration of our implementation of 3D photoelectron VMI, we performed a type of electron imaging experiment that would be impossible using the conventional inversion-based 2D VMI method. We photodissociated $(NO)_2$ and predominantly single-photon ionised the electronically-excited $NO(\mathrm{A}\,^2\Sigma^+)$ photoproducts, which are created in a 3s Rydberg state[36,40,41]:

$$\mathrm{NO}\,(\mathrm{A}\,^2\Sigma^+) + h\nu \rightarrow \mathrm{NO^+}\,(\mathrm{X}\,^1\Sigma^+) + e^-. \qquad (3)$$

Single photon ionization of this state produces a 0.84 eV nearly-pure p-wave photoelectron distribution with a lab-frame orientation that is entirely determined by the probe laser polarization, since the

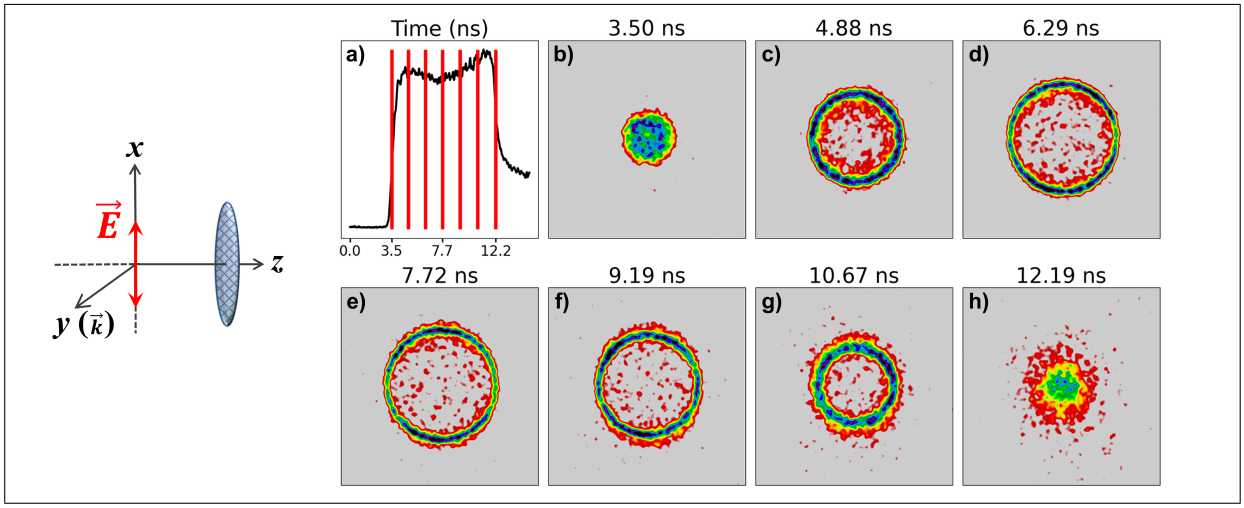

FIG. 9. Time-stamped 3D electron VMI data recorded following two-photon ionization of xenon at 200 nm, resulting in a photoelectron distribution with a peak signal intensity at 0.27 eV. A ~4.3 V/cm extraction field was implemented, resulting in an electron time spread of 8.8 ns. The coordinate system shown to the left highlights the experimental geometry, with the polarization vector of the linearly-polarised light aligned along the x-axis, the propagation axis of the laser ($\vec{k}$) along the y-axis, and the TOF axis (z) directed toward the MCP detector. (a) Photoelectron yield over time at the detector, with vertical lines indicating the time bins used in the following slices. (b)-(h) A few exemplary time slices of the 3D photoelectron distribution through the x-y plane, constructed by binning the processed (x, y, t) data by arrival time and smoothing to highlight the qualitative features. Panel (b) shows electrons emitted toward the detector (earliest to arrive) and (h) shows electrons emitted away from the detector (latest to arrive). Each slice has a temporal width equal to our experimental time resolution (160 ps). A video of this data set is available as supplementary material.

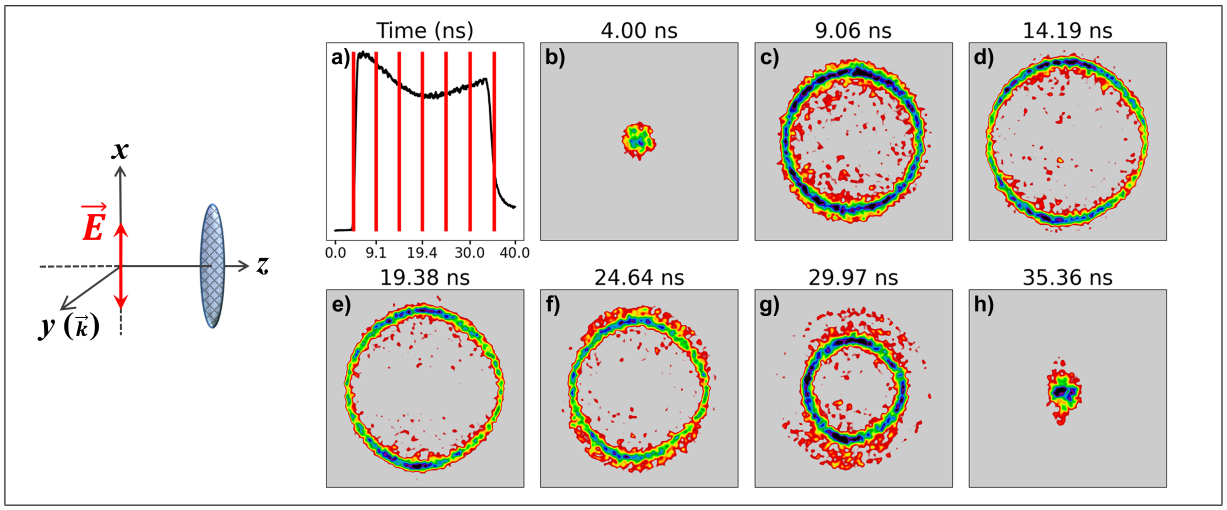

FIG. 10. Time-stamped 3D electron VMI data recorded following two-photon ionization of xenon at 200 nm, resulting in a photoelectron distribution with a peak signal intensity at 0.27 eV. A ~1.6 V/cm extraction field was implemented here, resulting in an electron time spread of 31 ns. The coordinate system on the left highlights the experimental geometry, as in Fig. 9. (a) Photoelectron yield over time at the detector, with vertical lines indicating the time bins used in the following slices. (b)-(h) A few exemplary time slices of the 3D photoelectron distribution through the x-y plane, constructed by binning the processed (x, y, t) data by arrival time and smoothing to highlight the qualitative features. Each slice has a temporal width equal to our experimental time resolution (160 ps).

initially-formed photoproduct Rydberg state is spherically symmetric[36,42]. To demonstrate that this 3D VMI measurement does not constrain the probe laser polarization to lie in the detector plane, as required for inversion-based 2D VMI, we collected data sets at three different probe polarization geometries. The polarization angles we used were $\theta = 0°$, 45° and 90°, where θ (defined in Fig. 12) is measured from the z-axis. The average hit counts for these data sets were 1.9 ($\theta = 0°$), 2.1 ($\theta = 45°$), and 3.1 ($\theta = 90°$) hits/shot. These experiments were performed

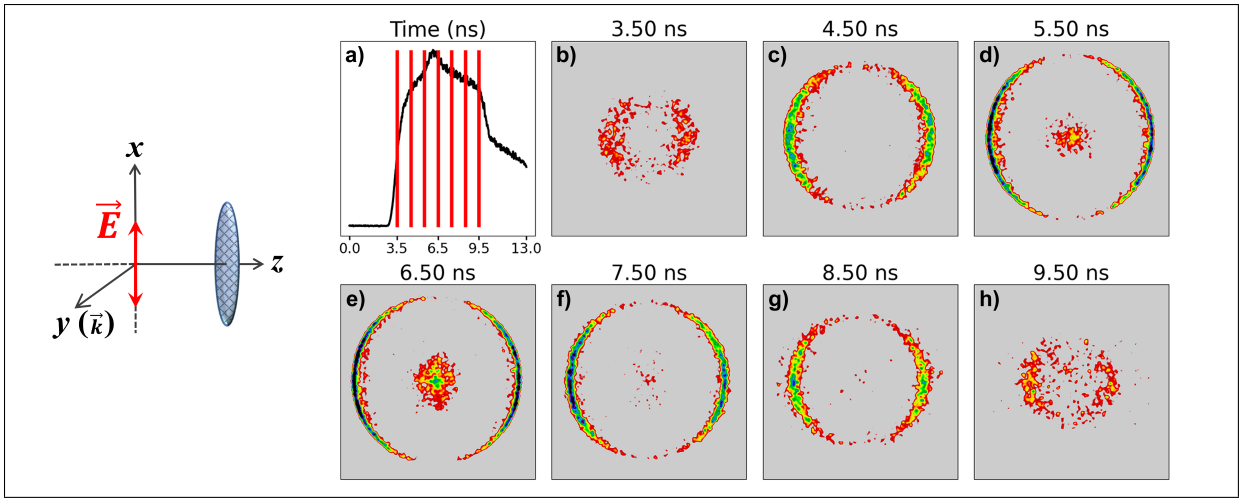

FIG. 11. Time-stamped 3D electron VMI data recorded following two-photon ionization of CH_3I at 200 nm, resulting in a photoelectron distribution with a peak signal intensity at 2.78 eV. A ~16 V/cm extraction field was implemented here, resulting in an electron time spread of 6.9 ns. The coordinate system on the left highlights the experimental geometry, as in Fig. 9. (a) Photoelectron yield over time at the detector, with vertical lines indicating the time bins used in the following slices. (b)-(h) A few exemplary time slices of the 3D photoelectron distribution through the x-y plane, constructed by binning the processed (x, y, t) data by arrival time and smoothing to highlight the qualitative features. Each slice has a temporal width equal to our experimental time resolution (160 ps).

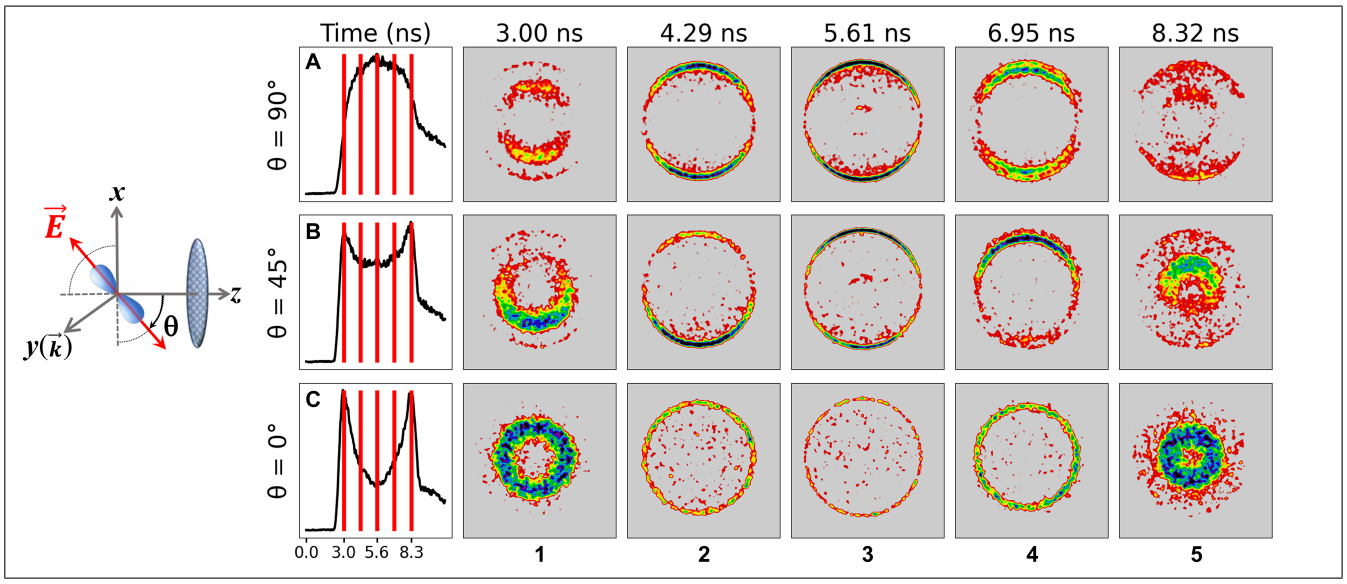

FIG. 12. Time-stamped 3D VMI data for photodissociation of $(NO)_2$ at 213 nm and subsequent photoionization of the NO(A) photoproducts at 266 nm, resulting in a photoelectron distribution with a peak signal intensity at 0.84 eV. An ~11 V/cm extraction field was implemented here, resulting in an electron time spread of 6.2 ns. This ionization scheme produces a nearly-pure p-wave photoelectron distribution aligned with the probe laser polarization $\vec{E}$ (at angle θ with the z-axis), as shown in the coordinate system to the left, where y ($\vec{k}$) is the laser propagation direction and z is the TOF axis. To demonstrate our 3D electron VMI capability, we used three linear polarization cases: θ = 0° (bottom row), 45° (middle row), and 90° (top row). The 90° case is the only one accessible to conventional inversion-reliant 2D VMI. The first image on each row shows the photoelectron yield plotted as a function of time for each case. The images to the right of these plots show a few exemplary time slices of the 3D photoelectron distribution through the x-y plane, constructed by binning the processed (x, y, t) data by arrival time and smoothing to highlight the qualitative features. Each slice has a temporal width equal to our experimental time resolution (160 ps) and is centered at the times indicated by the red vertical lines in the left panels (and noted at the top of each column). Column 1 (labelled along the bottom) shows electrons emitted toward the detector (earliest to arrive) and column 5 shows electrons emitted away from the detector (latest to arrive). A video of the 45° data set is available as supplementary material.

with an intermediate level of time-stretching, giving a time spread of 6.2 ns. Note that the same 3D photoelectron distribution was measured in each of these experiments, with each individually and directly yielding the full 3D photoelectron distribution. This should be contrasted with tomographic 3D photoelectron distribution reconstruction approaches, which extract similar information via a series of experiments performed with multiple laser polarization geometries[43,44] which unavoidably and significantly increases the duration of the measurement.

In Fig. 12, we present the analysed and time-stamped NO data as three rows of time slices through the 3D photoelectron distribution, with each row corresponding to the result of a different experiment, performed with a different polarization geometry. The $\theta = 90^\circ$ configuration (top row) corresponds to the same ionizing polarization geometry used in the Xe and CH_3I photoionization experiments. This is also one of the polarization geometries required in conventional inversion-based 2D VMI experiments. The lobes of the photoelectron angular distribution are directed along the x-axis, for which we expect to see an electron yield which peaks at the centre of the distribution and is less intense at either end. We also expect the electron yield to be highly localized along the ± x-axis where the lobes are located. These properties are clearly demonstrated in Fig. 12.

The $\theta = 0^\circ$ geometry (bottom row), with the laser polarization along the z (TOF) axis, is one that is not analyzable using conventional inversion-based 2D VMI. With this polarization geometry, we expect the photoelectron yield to be peaked on either end of the distribution and very weak near the centre where the node of the nearly-pure p-wave distribution is located. We also expect the distribution to be cylindrically symmetric about the z-axis with no anisotropy visible for the presented x-y slices. These expectations are satisfied. The presence of some photoelectron density in Fig. 12 (C3) is an expected result of the imperfect nature of the p-wave distribution[42].

With the $\theta = 45^\circ$ data set (middle row), we demonstrate our ability to image 3D photoelectron distributions produced using arbitrary polarization geometries in a single experiment. We set the polarization to be at 45° between the x and z axes, so that the photoelectron distribution is concentrated in the negative x-axis for the front of the distribution (the earliest arriving electrons) while shifting gradually toward the positive x-axis at the back end (late electron arrival times). As shown in Fig. 12, we observe the expected result: at the front end of the distribution (panels B1 and B2) the electrons are concentrated in the lower part of the images (the negative x-axis), and at the back end (panels B4 and B5) the electrons concentrated in the top of the image (positive x-axis). At the centre of the distribution (panel B3), the electron yield is evenly split between the top and bottom. The total electron yield over time (row B, left side) also agrees with expectations, as its qualitative structure lies roughly between the $\theta = 0^\circ$ and $\theta = 90^\circ$ cases.

In Fig. 12, a lower-energy photoelectron signal is also present, most visible in column 3 (middle time slice). The energy of this ring is about 0.055 eV, allowing us to assign this feature to the 2-photon ionization of ground state NO(X) at 266 nm. This is likely since NO(X) monomers form the overwhelming majority of species in the molecular beam and given that each NO(A) photoproduct is produced together with an NO(X) cofragment in the 213 nm photodissociation of $(NO)_2$.

The polarization geometry of the $\theta = 90^\circ$ data set allows for both inversion- and slice-based analyses. Using the 3D data, we extracted centre slices in the x-y, x-z, and y-z planes. Preparation of the x-z and y-z slices required a transformation of the slice data from (x, y, t) to (x, y, z) coordinates, such that the transformed coordinates form a sphere. This was accomplished by fitting each half of the data (forward- and backward-emitted electrons) to an ellipse and transforming each using the fit. In Fig. 13 (a) we compare the photoelectron spectra derived from the inverted data and the x-y slice. We achieve a better energy resolution ($\Delta E/E$) using the x-y slice (2.2%) than with the inversion (3.8%). In Fig. 13 (b) we show the photoelectron angular distributions (PADs) of the inverted data and all three slices (x-y, x-z, y-z). Each PAD has been fitted to obtain asymmetry parameters (β_{20}/β_{00}). The results for the inverted, x-y slice, and x-z slice are consistent with previous work[42,46], which reported values between 1.2 and 1.7. The y-z slice for the $\theta = 90^\circ$ being considered here is expected to be angle invariant as a result of the cylindrical symmetry of the distribution. Thus, we expect an asymmetry parameter of zero, which nearly agrees with our experimental result of 0.13±0.06. This deviation is most likely caused by the dip in intensity near 90° in the PAD, which is an expected result of gain degradation at the centre region of our MCP detector.

V. CONCLUSION

Multi-hit 3D photoelectron VMI is of interest because it is not reliant on 2D-projection inversion algorithms that restrict the variation of the laser polarization geometries. Neither does it rely on the performance of multiple experiments with different polarisation geometries and tomographic reconstruction of the 3D electron distribution. It also represents a high data rate alternative to 3D photoelectron imaging techniques using delay-line anodes. The advantages afforded by 3D photoelectron VMI will permit a variety of novel time-resolved linear and circular dichroism experiments, as well as the use of non-symmetric rotational wavepacket revivals for the reconstruction of Molecular Frame Photoelectron Angular Distibutions (MFPADS)[47,48]. Here we presented a time-stretched, multi-hit 3D photoelectron VMI instrument using a 13-electrode lens design. Our simple CMOS-camera-based approach maintains good VMI fo-

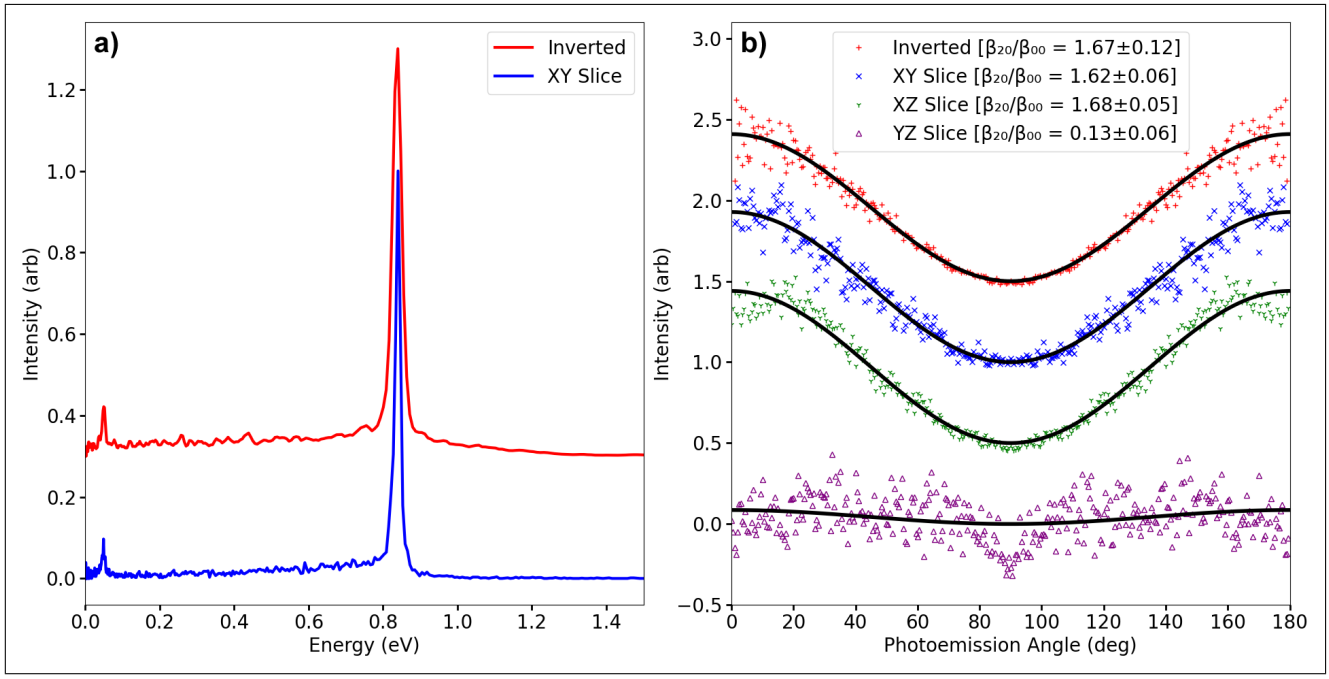

FIG. 13. Photoelectron spectra (a) and photoelectron angular distributions (b) for the single photon photodissociation of $(NO)_2$ at 213 nm and subsequent single photon photoionization of the NO(A) and NO(X) photoproducts at 266 nm (high-intensity and low-intensity peaks, respectively). The data shown here correspond to the inversion-compatible 90° (detector plane) probe polarization case (as defined in Fig. 12). In (a), we present the spectra of both the Abel-inverted image (red) and the central x-y slice (blue), which yield energy resolutions ($\Delta E/E$) of 3.7% and 2.1%, respectively. In (b), we present the angular distributions and fitted asymmetry parameters (β_{20}/β_{00}) for the Abel-inverted[45] image (1.67±0.12) x-y slice (1.62±0.06), x-z slice (1.68±0.05), and y-z slice (0.13±0.06). In these plots, the emission angle is measured from the positive x-axis for the inverted, x-y, and x-z slices, but from the positive y-axis for the y-z slice. The stated errors represent 95% confidence intervals. The dip in intensity near 90° in the y-z slice is a result of gain degradation at the very center of the detector. In both (a) and (b), the plots are displaced vertically for visibility proposes.

cusing conditions and, importantly, is capable of both 3D and 2D VMI operation. Test data were collected using photoelectrons with kinetic energies ranging from 0.27 to 2.78 eV, although good performance up to 10 eV is expected. Time-stretching of 31 and 6.9 ns was achieved for the 0.27 and 2.78 eV electrons, respectively. Rotation of the probe laser polarization axis through non-cylindrically-symmetric geometries clearly demonstrated the advantages of 3D over 2D VMI. An analysis of the multi-hit capability of the instrument and associated data processing shows that time stretching provides a significant improvement, yielding correct (x, y, t) assignment of more than 6 hits per laser shot with near-maximum stretching.

We are implementing a number of improvements for the near future. The multi-hit assignment of the temporal (digitizer) and spatial (camera) coordinates can be improved by using an MCP detector having both a higher average gain and a broader pulse height distribution. The current time resolution of 160 ps is partially due to electronic timing jitter, which can be reduced by co-adding an accurately timed photodiode signal from the laser to the GHz digitizer electron time-of-flight record.

For especially low photoelectron kinetic energies and implemented extraction field gradients, the loss of circular symmetry observed for large time-stretching is due to the four-fold broken symmetry of the laser port electrode. We anticipate approximate correction of this via the use of additional electrodes and small local field tuning centred on each port-electrode hole. We are currently building a second-generation time-stretching 3D VMI instrument that will include a collinear Wiley-McLaren time-of-flight mass spectrometer, as was previously demonstrated[27], allowing us to perform photoion-photoelectron image covariance VMI.

The data analysis procedures described above are being further refined. The problem of assigning the multi-hit data, particularly when multiple ambiguous assignments are available, is a complex one which warrants a proper statistical treatment. Finally, the 3D (x, y, t) data presented here must be transformed into initial recoil momentum vectors for practical use. As the electron extraction field lines are curved, this requires detailed analysis[49,50]. We look forward to future developments in 3D photoelectron VMI, here and in research groups around the world, which will further its use in time- and energy-resolved atomic and molecular photoionization experiments.

SUPPLEMENTARY MATERIAL

See supplementary material for videos showing the time-resolved 3D VMI data sets from the Xe $5p^6(^1S_0)$ and the NO($A\,^2\Sigma^+$) at 45° photoionization experiments.

ACKNOWLEDGEMENTS

The authors thank Prof. Wen Li (Wayne State) for his encouragement and support of this work. We thank the NSERC Discovery Grants and Postgraduate Scholarships – Doctoral programs, the Canada Foundation for Innovation, the Canada Research Chairs, the NRC-uOttawa Joint Centre for Extreme Photonics (JCEP), and the NRC CSTIP Quantum Sensors project QSP-075-1 for financial support.

AUTHOR DECLARATIONS

Conflict of Interest

The authors have no conflicts to disclose.

Author Contributions

SG, AB, DM, and IW performed the bulk of the experiment and analysis with assistance from RL and VM. IW and AS conceived the experiment. IW and MH performed SIMION simulations. IW designed the electrostatic lens and VMI chamber. IW and AB built the apparatus. All authors contributed in discussion and preparation of the manuscript.

Scott Goudreau: Conceptualization (equal); Formal analysis (equal); Methodology (equal); Writing – review & editing (equal). **Andrey E. Boguslavskiy**: Conceptualization (equal); Formal analysis (equal); Methodology (equal); Writing – review & editing (equal). **Doug Moffatt**: Methodology (equal); Formal analysis (equal). **Varun Makhija**: Methodology (equal). **Michael Hemsworth**: Formal analysis (equal); Methodology (equal). **Rune Lausten**: Methodology (equal). **Claude Marceau**: Methodology (equal). **Iain Wilkinson**: Conceptualization (equal); Methodology (equal); Data curation (equal); Writing – review & editing (equal). **Albert Stolow**: Conceptualization (equal); Data curation (equal); Funding acquisition; Project administration; Supervision; Writing – review & editing (equal).

DATA AVAILABILITY

The data that support the findings of this study are available from the corresponding authors upon reasonable request.

REFERENCES

[1]A. T. J. B. Eppink and D. H. Parker, Rev. Sci. Instrum. **68**, 3477 (1997).
[2]M. N. R. Ashfold, N. H. Nahler, A. J. Orr-Ewing, O. P. J. Vieuxmaire, R. L. Toomes, T. N. Kitsopoulos, I. A. Garcia, D. A. Chestakov, S.-M. Wu, and D. H. Parker, Phys. Chem. Chem. Phys. **8**, 26 (2006).
[3]M. H. M. Janssen and I. Powis, Phys. Chem. Chem. Phys. **16**, 856 (2014).
[4]M. N. R. Ashfold and D. H. Parker, Phys. Chem. Chem. Phys. **16**, 381 (2014).
[5]D. M. Neumark, J. Phys. Chem. A **112**, 13287 (2008).
[6]A. G. Suits, Rev. Sci. Instrum. **89**, 111101 (2018).
[7]M. J. J. Vrakking, Phys. Chem. Chem. Phys. **16**, 2775 (2014).
[8]R. Mabbs, E. R. Grumbling, K. Pichugin, and A. Sanov, Chem. Soc. Rev. **38**, 2169 (2009).
[9]D. W. Chandler and P. L. Houston, J. Chem. Phys. **87**, 1445 (1987).
[10]G. Basnayake, Y. Ranathunga, S. K. Lee, and W. Li, J. Phys. B **55**, 023001 (2022).
[11]D. Townsend, M. P. Minitti, and A. G. Suits, Rev. Sci. Instrum. **74**, 2530 (2003).
[12]J. J. Lin, J. Zhou, W. Shiu, and K. Liu, Rev. Sci. Instrum. **74**, 2495 (2003).
[13]W. Li, S. D. Chambreau, S. A. Lahankar, and A. G. Suits, Rev. Sci. Instrum. **76**, 063106 (2005).
[14]S. Kauczok, N. Gödecke, A. I. Chichinin, M. Veckenstedt, C. Maul, and K.-H. Gericke, Rev. Sci. Instrum. **80**, 083301 (2009).
[15]O. Jagutzki, A. Cerezo, A. Czasch, R. Dorner, M. Hattas, M. Huang, V. Mergel, U. Spillmann, K. Ullmann-Pfleger, T. Weber, H. Schmidt-Bocking, and G. Smith, IEEE Transactions on Nuclear Science **49**, 2477 (2002).
[16]S. K. Lee, F. Cudry, Y. F. Lin, S. Lingenfelter, A. H. Winney, L. Fan, and W. Li, Rev. Sci. Instrum. **85**, 123303 (2014).
[17]S. K. Lee, Y. F. Lin, S. Lingenfelter, L. Fan, A. H. Winney, and W. Li, J. Chem. Phys. **141**, 221101 (2014).
[18]Y. F. Lin, S. K. Lee, P. Adhikari, T. Herath, S. Lingenfelter, A. H. Winney, and W. Li, Rev. Sci. Instrum. **86**, 096110 (2015).
[19]L. Fan, S. K. Lee, Y.-J. Tu, B. Mignolet, D. Couch, K. Dorney, Q. Nguyen, L. Wooldridge, M. Murnane, F. Remacle, H. B. Schlegel, and W. Li, J. Chem. Phys. **147**, 013920 (2017).
[20]A. H. Winney, S. K. Lee, Y. F. Lin, Q. Liao, P. Adhikari, G. Basnayake, H. B. Schlegel, and W. Li, Phys. Rev. Lett. **119**, 123201 (2017).
[21]Q. Liao, A. H. Winney, S. K. Lee, Y. F. Lin, P. Adhikari, and W. Li, Phys. Rev. A **96**, 023401 (2017).
[22]C. Weeraratna, C. Amarasinghe, S. K. Lee, W. Li, and A. G. Suits, J. Chem. Phys. **149**, 084202 (2018).
[23]X. Urbain, D. Bech, J.-P. Van Roy, M. Géléoc, S. J. Weber, A. Huetz, and Y. J. Picard, Rev. Sci. Instrum. **86**, 023305 (2015).
[24]A. Zhao, M. van Beuzekom, B. Bouwens, D. Byelov, I. Chakaberia, C. Cheng, E. Maddox, A. Nomerotski, P. Svihra, J. Visser, V. Vrba, and T. Weinacht, Rev. Sci. Instrum. **88**, 113104 (2017).
[25]D. A. Debrah, G. A. Stewart, G. Basnayake, A. Nomerotski, P. Svihra, S. K. Lee, and W. Li, Rev. Sci. Instrum. **91**, 023316 (2020).
[26]C. Cheng, G. Moğol, T. Weinacht, A. Nomerotski, and C. Trallero-Herrero, Rev. Sci. Instrum. **93**, 013003 (2022).
[27]M. Davino, E. McManus, N. G. Helming, C. Cheng, G. Mogol, Z. Rodnova, G. Harrison, K. Watson, T. Weinacht, G. N. Gibson, T. Saule, and C. A. Trallero-Herrero, Rev. Sci. Instrum. **94**, 013303 (2023).
[28]R. Ballabriga, M. Campbell, and X. Llopart, Nucl. Instrum. Methods Phys. Res. A **878**, 10 (2018).
[29]X. Llopart, J. Alozy, R. Ballabriga, M. Campbell, R. Casanova, V. Gromov, E. Heijne, T. Poikela, E. Santin, V. Sriskaran,

L. Tlustos, and A. Vitkovskiy, J. Instrum. **17**, C01044 (2022).
[30]N. G. Kling, D. Paul, A. Gura, G. Laurent, S. De, H. Li, Z. Wang, B. Ahn, C. H. Kim, T. K. Kim, I. V. Litvinyuk, C. L. Cocke, I. Ben-Itzhak, D. Kim, and M. F. Kling, J. Instrum. **9**, P05005 (2014).
[31]I. Wilkinson, Ph.D. thesis, University of Leeds (2010).
[32]S.-Y. Liu, K. Alnama, J. Matsumoto, K. Nishizawa, H. Kohguchi, Y.-P. Lee, and T. Suzuki, J. Phys. Chem. A **115**, 2953 (2011).
[33]M. Hemsworth, Master's thesis, University of Ottawa (2020).
[34]U. Even, EPJ Tech. Instrum. **2**, 17 (2015).
[35]European Machine Vision Association (EMVA), Release 4.0 General, www.emva.org (2020).
[36]O. Geßner, A. M. D. Lee, J. P. Shaffer, H. Reisler, S. V. Levchenko, A. I. Krylov, J. G. Underwood, H. Shi, A. L. L. East, D. M. Wardlaw, E. t. H. Chrysostom, C. C. Hayden, and A. Stolow, Science **311**, 219 (2006).
[37]O. J. Clarkin, Ph.D. thesis, Queen's University (2012).
[38]C. Heckenkamp, F. Schäfers, G. Schönhense, and U. Heinzmann, Z. Phys. D **2**, 257 (1986).
[39]N. Thire, R. Cireasa, V. Blanchet, and S. T. Pratt, Phys. Chem. Chem. Phys. **12**, 15644 (2010).
[40]A. V. Demyanenko, A. B. Potter, V. Dribinski, and H. Reisler, J. Chem. Phys. **117**, 2568 (2002).
[41]V. Blanchet and A. Stolow, J. Chem. Phys. **108**, 4371 (1998).
[42]M. Tsubouchi, C. de Lange, and T. Suzuki, J. Electron Spectrosc. Relat. Phenom. **142**, 193 (2005).
[43]M. Wollenhaupt, M. Krug, J. Koehler, T. Bayer, C. Sarpe-Tudoran, and T. Baumert, Appl. Phys. B: Lasers Opt. **95**, 647 (2009).
[44]C. Sparling and D. Townsend, J. Chem. Phys. **157**, 114201 (2022).
[45]Y. T. Cho and S.-J. Na, Meas. Sci. Technol. **16**, 878 (2005).
[46]T. Horio and T. Suzuki, Rev. Sci. Instrum. **80**, 013706 (2009).
[47]C. Marceau, V. Makhija, D. Platzer, A. Y. Naumov, P. B. Corkum, A. Stolow, D. M. Villeneuve, and P. Hockett, Phys. Rev. Lett. **119**, 083401 (2017).
[48]M. Gregory, P. Hockett, A. Stolow, and V. Makhija, J. Phys. B **54**, 145601 (2021).
[49]M. Lebech, Ph.D. thesis, Universite Paris-Sud (2003).
[50]F. Allum, R. Mason, M. Burt, C. S. Slater, E. Squires, B. Winter, and M. Brouard, Mol. Phys. **119**, e1842531 (2021).